Trace element composition and U-Pb ages of cassiterite from the Bolivian tin belt

Laura Gemmrich, Lisard Torró, Joan Carles Melgarejo, Oscar Laurent, Jean Vallance, Cyril Chelle-Michou, Thierry Sempere

Trace element composition and U-Pb ages of cassiterite from the Bolivian tin belt

Laura Gemmrich[a], Lisard Torró[b,*], Joan Carles Melgarejo[a], Oscar Laurent[c], Jean Vallance[b], Cyril Chelle-Michou[c], Thierry P.A. Sempere[d]

[a] *Departament de Mineralogia, Petrologia i Geologia Aplicada, Universitat de Barcelona (UB), C/Martí i Franquès s/n, 08028 Barcelona, Spain*

[b] *Geological Engineering Program, Faculty of Sciences and Engineering, Pontifical Catholic University of Peru (PUCP), Av. Universitaria 180, San Miguel, Lima 15088, Peru*

[c] *ETH Zürich, Department of Earth Sciences, Institute for Geochemistry and Petrology, 8092 Zürich, Switzerland*

[d] *Consultant and Exploration Manager at ANDES C&P, Lima, Peru*

To be submitted to *Mineralium Deposita*

[*]Corresponding author: Dr. Lisard Torró

E-mail address: lisardtorro@hotmail.com

Phone: (+51) 6262000 Ext. 5060

Abstract

The Bolivian tin belt is a metallogenic province in the Eastern Cordillera of the Andes known for its Sn, W, Ag and base metal deposits. Cassiterite, which is a major constituent in many magmatic-hydrothermal ore deposits from the Bolivian tin belt, can incorporate dozens of elements within its crystal lattice, making it a useful geological tracer mineral, and also a potential host of critical elements. New U-Pb dating of cassiterite yields Late Triassic (Kellhuani deposit) and Late Oligocene to earliest Miocene (Viloco, Huanuni and Llallagua deposits) ages. These ages confirm that Sn mineralization in the Bolivian tin belt occurred at least in two separate events during two major magmatic episodes apparently triggered by mantle upwelling, decompression melting and basalt

production promoting high heat flow into the overlying crust. The composition of studied hydrothermal cassiterite yields some geochemical trends that are attributed to its distance to the causative intrusion and/or level of emplacement. For example, cassiterite is generally enriched in Nb and Ta and yields higher Ti/Zr and Ti/Sc ratios in samples from xenothermal ore deposits located adjacent to intrusive complexes relative to shallow xenothermal and epithermal ore deposits. Therefore, these geochemical trends in cassiterite are useful tracers pointing to magmatic-hydrothermal centers. REE distribution in cassiterite was likely influenced by boiling processes, which resulted in tetrad-type irregularities. Cassiterite from the Bolivian tin belt is unattractive as a source for Nb (interquartile range [IQR] 4.84-0.037 ppm), Ta (IQR 0.0924-0.0126 ppm) and Ge (IQR 3.92-0.776 ppm). Some deposits, however, contain cassiterite relatively enriched in In (IQR 96.9-9.78 ppm, up to 1414 ppm) and Ga (IQR 92.1-3.03, up to 7437 ppm), that could constitute an attractive supplementary source for these elements in addition to sulfide minerals in the same deposits.

Keywords: Central Andes, geochemical composition, high-tech metals, critical elements, U-Pb geochronology

Introduction

Cassiterite, a tin oxide mineral (SnO_2) of the rutile group and the primary Sn ore mineral, can incorporate a wealth of elements in minor and trace concentrations within its structure. Typical elements that are present in significant, although variable, amounts within its crystal lattice include Fe, Ti, Mn, Al, Nb, Ta and U, which substitute for Sn cations. Innovation in analytical chemistry (i.e., ICP-MS and micro-PIXE; e.g., Plimer et al. 1991; Serranti et al. 2002) further allows the determination of other elements found in trace amounts in cassiterite such as those of the rare earth elements (REE), Be and In amongst others. Some of these elements (e.g., Nb, Ta, W, REE, Be and In) are considered high-tech metals critical to the global economy (Skirrow et al. 2013; European Commission 2017; Schulz et al. 2017).

The broad range of P-T-X conditions in which cassiterite forms, its strong physical and chemical resistance and its plethora of chemical constituents including both compatible and incompatible elements makes this mineral useful as a petrogenetic indicator (Murciego et al. 1977; Plimer et al. 1991; Serranti et al. 2002; Jiang et al. 2004; Chen et al. 2019). Furthermore, the moderate U^{4+} and low Pb^{2+} contents and high Pb isotope closure temperature (up to 860ºC; Zhang et al. 2011) in cassiterite makes it suitable for U-Pb dating (e.g., Zhang et al. 2017, 2019; Guo et al. 2018; Neymark et al. 2018; Chen et al. 2019; Cheng et al. 2019; Kendall-Langley et al. 2019; Moscati and Neymark 2019; Zhao et al. 2019; Legros et al. 2020; Lehmann et al. 2020; Mao et al. 2020).

The Bolivian tin belt, in the Central Andes, is one of the largest tin metallogenic belts worldwide and in 2019 accounted for about 6% of the global tin production; in addition, it produced about 5% of silver and 1.5% of tungsten globally (U.S. Geological Survey 2020). Despite massive tin production since early 1900s, by when most Bolivian great tin deposits had been discovered, Bolivia is estimated to contain > 8% of the world's tin reserves (Arce-Burgoa and Goldfarb 2009; U.S. Geological Survey 2020). However, a detailed survey on the geochemical composition of cassiterite from this metalliferous belt has never been conducted. Furthermore, the age of the magmatism along the Bolivian tin belt is relatively well constrained through U-Pb zircon dating, but dispersion of K-Ar and Ar-Ar mica and feldspar dates reveals a complex thermal history (Ahfeld 1967; Clark and Farrar 1973; Evernden et al. 1977; Grant et al. 1979; McBride et al. 1983; Clark et al. 1990; Sugaki et al. 2003; Gillis et al. 2006; Cordani et al. 2019). This is especially the case in the northern segment of the Bolivian tin belt, where plutons of Triassic age cluster. As previous geochronological studies on tin deposits were mainly based on K-Ar and Ar-Ar dating of hydrothermal mica, some questions remain in respect of their reliability. In this study we determine the geochemical composition and U-Pb dates of cassiterite grains from nine deposits/districts of the Bolivian tin belt with a threefold aim: i) to refine the geochronology of tin mineralization in this region, ii) to constrain the mechanisms that control minor and trace element concentrations in cassiterite crystallized at contrasting conditions within the xenothermal (i.e., polymetallic high-temperature [~300-500ºC] vein-type deposits emplaced in the sub-epithermal environment; Buddington 1935, Imai et al. 1975, Heuschmidt et al. 2002) and epithermal environments, and iii) to assess their potential as source of high-tech byproducts.

Geological setting

Geological setting of the Bolivian Andes

The ore deposits dated in this paper are located in the northern and central segments of the Bolivian Eastern Cordillera. These segments are parts of the northwest limb of the Bolivian Orocline (Isacks 1988), and, more precisely, of its southernmost portion, i.e. close to the oroclinal "core hinge". This broad region therefore shares many geological characteristics with adjacent Peru, and the descriptions and comments in this section are often envisioned from this point of view.

The Bolivian Andes present a marked morphotectonic partition that reflects differences in geological history, paleostructural domains and current crustal structure. These domains are, from west to east, the Western Cordillera, the Altiplano and the Eastern Cordillera. Furthermore, a deformed "Subandean Belt" serves as a

tectonic transition between the Eastern Cordillera and the nearly undeformed Amazonian Lowlands to the northeast and east.

The Western Cordillera corresponds to the present-day location of the main magmatic arc related to subduction processes. It is characterized by a ~100 km-wide belt of volcanoes sitting on a high-altitude surface, which reflects a considerable crustal thickness beneath (e.g., James 1971a,b; Isacks 1988; Kono et al. 1989; Lamb and Hoke 1997). At the latitudes of Bolivia, the Western Cordillera however extends also in adjacent Northern Chile. It is mostly composed of Late Miocene to recent intermediate to felsic igneous rocks that intruded in and extruded over Jurassic and Cretaceous sedimentary and volcanic rocks. The igneous rocks from the Western Cordillera belong to the magnetite series and record a high contribution of a mantle component (Ishihara 1981; Sugaki et al. 1988a).

The upper crustal structure of the Altiplano varies significantly. It seems likely that its lower crust has been thickened through ductile flow from the overthickened crust along both the Western and Eastern cordilleras (Husson and Sempere 2003). Much of the current Altiplano surface is covered by recent sedimentary and volcanic deposits; it is strongly suspected that its eastern fringe corresponds to the buried western fringe of the Eastern Cordillera, and thus constitutes a transitional strip between the two domains. In particular, this transition is confirmed by the observation that many magmatic phenomena that affected the Altiplano also affected the crust of the western Eastern Cordillera, along which products of coeval and related magmatism are commonly observed (see below).

The scope of this paper is focused on the Eastern Cordillera since it hosts the Bolivian tin belt. The Eastern Cordillera was formed by inversion and substantial shortening of a Triassic rift system (Sempere 2000; Sempere et al. 2002). This protracted compressional to transpressional deformation has developed since the Eocene and/or Oligocene in relation to the formation of the Bolivian Orocline (e.g., Farrar et al. 1988; Sempere et al. 1990; Roperch et al. 2006), and the ensuing erosion has resulted in the exposure of mainly Ordovician and Silurian strata, which as a whole may be over ~10 km thick.

The almost exclusively marine stratigraphic set formed by the Ordovician to Devonian strata is so thick that it raises the question of the geotectonic context in which this succession accumulated, and, indirectly, that of the time at which subduction was initiated at the latitude of Bolivia and Peru. Both present-day territories were part of supercontinents Rodinia and Pannotia; Laurentia separated from the latter at the latitudes of Peru and Bolivia through the opening of the Iapetus Ocean during the latest Neoproterozoic (Scotese 2009), which implies that what

was to become the Central Andean margin is very likely to have been passive at least in the earliest Paleozoic. A subduction-arc geochemical signature is however unambiguously noted in Carboniferous plutons of Peru (Mišković et al. 2009), which provides a minimum age for the onset of subduction at these latitudes.

The overall geological evolution of Bolivia has been summarized by Sempere (1995), who divided the stratigraphic record into a number of supersequences that reflect major changes in tectonic context. This preliminary understanding has been refined since that time, in particular thanks to new data from Bolivia and especially Peru. The Carboniferous arc orogeny that developed along at least the Eastern Cordillera of Peru was followed in the Permian by the extensional collapse of the resulting overthickened crust (Mišković et al. 2009).

Extensional conditions considerably increased in the Middle to Late Triassic, and resulted in the development of a major back-arc rift system (Sempere et al. 2002; Spikings et al. 2016). During the "Mitu time interval" (~240–220 Ma), such an intense extension and associated mantle-derived mafic magmatism are likely to have generated an anomalously high heat flow. Late Triassic crustal anatexis is documented in several areas of contiguous E and SE Peru (see Kontak et al. 1990); in the NW-trending segment of the Eastern Cordillera of Bolivia, anatexis is recorded by the Zongo-Yani batholith (Fig. 1A), which consists of two-mica granite plutons that are commonly foliated; the peraluminous composition points to an anatectic origin, and the foliation indicates extensional shearing conditions during magma emplacement. In the Cuticucho-Samaini area, which is located ~25 km north of the Milluni Sn-Zn deposit (Fig. 1A), the Zongo-Yani batholith locally displays facies that range from pervasively foliated to weakly foliated, whereas its composition varies from monzogranite to syenogranite (Farrar et al. 1990). U-Pb zircon dating yielded dates of 222.2 –9.1/+7.7 and 225.1 –4.4/+4.1 Ma on the pervasively and weakly foliated facies, respectively (the weighted mean of these dates is 224.5 –4.0/+3.6 Ma). The U-Pb work confirmed that zircons from this pluton had been recycled by anatexis, and these dates are based on lower intercepts in the respective concordia diagrams (Farrar et al. 1990); all zircons that Gillis et al. (2006) attempted to date by the U-Pb method were also found to be discordant and gave $^{206}Pb/^{238}U$ dates between 263 and 226 Ma for the Zongo pluton.

The Triassic rifting led to the subsequent accumulation of a stratigraphic succession that ranges well into the Jurassic (Sempere et al. 2002). After an apparently long sedimentation hiatus, deposition resumed at ~100 Ma; a significant increase in subsidence took place at ~90 Ma, reflecting the coeval growth of the main magmatic arc (Sempere 1994; Demouy et al. 2012). The latest Cretaceous to Eocene stratigraphic record mainly consists of red

136 beds forming a monotonous succession that may be several km thick (Sempere et al. 1997; Horton 2001),
137 interpreted as a classical foreland basin (e.g., DeCelles and Horton 2003).

138 Arc migration is best recorded in southern Peru. Mamani et al. (2010) and Demouy et al. (2012) showed that in
139 this large region the arc, from a position currently offshore, migrated northwards between ~130 and ~45 Ma to
140 occupy a position that coincides with the Andahuaylas-Yauri batholith south of Cuzco; the arc has migrated
141 "back" southwards since ~31–30 Ma (Mamani et al. 2010). Because the position of the arc is largely controlled by
142 the dip angle of the subducted slab, the latter back-migration must have implied a widening of the asthenospheric
143 wedge, which in turn involved mantle upwelling and thus decompression melting, and therefore the production of
144 large amounts of basaltic magma (Mamani et al. 2010). This logical chain is confirmed by the widespread
145 existence of basaltic magmatism of alkaline to shoshonitic composition centered over most of the Altiplano of
146 southern Peru and Bolivia, between ~31 and ~22 Ma in southern Peru (Kontak et al. 1996; Sandeman et al. 1995),
147 and between ~28 and ~21 Ma across the Bolivian Altiplano (Soler and Jiménez 1993); Fornari et al. (2002)
148 detected a diachronic onset of mafic volcanism from ~29 Ma in the southern Peruvian Altiplano to ~21-20 Ma in
149 the southernmost Bolivian Altiplano. The cumulated thickness of basaltic flows may locally be >2 km (Baldellón
150 et al. 1994), which eloquently illustrates the magnitude of the related mantle upwelling and thus anomalous heat
151 flow. The available dataset concerning this segment of the Bolivian Orocline suggests that mafic magmatism
152 extended beneath the entire Altiplano of southern Peru and Bolivia as well as adjacent areas, and that it has
153 continued through the Neogene and Quaternary, at least episodically at the surface.

154 In the Bolivian Altiplano, these mafic lavas occur as flows, sills, dikes and small intrusive stocks; thick and
155 extended flow breccias are common and suggest that many volcanic centers were active at that time (Fornari et al.
156 2002). Near the triple junction of Bolivia, Peru and Chile, the mafic Abaroa Formation yielded whole-rock ^{40}Ar-
157 ^{39}Ar dates comprised between 28.0 ± 0.1 and 27.3 ± 0.1 Ma (Fornari et al. 2002).

158 In the central Bolivian Altiplano, basaltic sills yielded whole-rock ^{40}Ar-^{39}Ar plateau dates of 24.2 ± 0.4 and 23.8 ±
159 0.1 Ma; the latter date was obtained on a >100 m-thick mafic sill characterized by plagioclase phenocrysts up to 3
160 cm in size (Fornari et al. 2002). About 75 km to the SSE, a ~1-km-thick section of red beds includes >15 basalt
161 levels; lava flows near the base and top of the section yielded whole-rock ^{40}Ar-^{39}Ar dates of 23.5 ± 0.1 and 23.6 ±
162 0.1 Ma, respectively, whereas a mafic dyke cutting several flows and sills yielded a plateau date of 23.5 ± 0.1 Ma;
163 these coinciding dates over a stratigraphic thickness of ~1 km indicate, again, that the corresponding mafic

164 magmatism was extremely productive at that time (~23.5 Ma in this case), and thus involved considerable mantle
165 upwelling, resulting decompression melting and a very high heat flow into the overlying crust.

166 Crustal thickening in the NW-trending region of the Bolivian Orocline has developed since ~30 Ma (Picard et al.
167 2008; Sempere et al. 2008 and references therein). The onset of crustal thickening thus coincided with the
168 widespread development of mafic magmatism during the Late Oligocene and earliest Miocene.

169 Unlike igneous rocks from the Western Cordillera, silicic intrusive and volcanic rocks from the Eastern Cordillera
170 of both Mesozoic (mostly ca. 225-200 Ma) and Tertiary (ca. 45-12.0 Ma) ages belong to the S-type, ilmenite series
171 and resulted from sediment melting in a thickened continental crust with up to 30% of mantle component (Sugaki
172 et al. 1981; Morgan et al. 1998; Lehmann et al. 2000; Mlynarczyk and Williams-Jones 2005; Maffione et al.
173 2009).

174 The morphotectonic provinces are juxtaposed by a succession of parallel, north to south trending mineralized belts
175 of Paleogene and Neogene ages. The Western Cordillera mostly comprises porphyry-type Cu-Mo-Au-Fe deposits,
176 the Altiplano, polymetallic vein- and replacement-type Cu-Pb-Zn-Ag deposits and sedimentary Cu deposits, and
177 the Eastern Cordillera, porphyry-type Sn-W-Ag deposits and associated polymetallic mineralization (Petersen
178 1970; Sillitoe 1972, 1976; Clark et al. 1990; Mlynarczyk and Williams-Jones 2005; Fontboté 2018). The existence
179 of metallogenic provinces (clusters of ore deposits with similar characteristics) in the Central Andes suggests
180 control by regional or large scale geologic environments or processes, which in the region were governed by the
181 quasi-continuous subduction along the western margin of the South American plate over the last ca. 300 My
182 (Clark et al. 1976, 1990; Sillitoe 1976; Lehmann et al. 1990; Mlynarczyk and Williams-Jones 2005; Wörner et al.
183 2018a,b; Fontboté 2018). In this convergent tectonic scenario, shortening, thickening and uplift favored the
184 accumulation of magma in the upper crust, which was responsible for the magmatic-hydrothermal activity that
185 formed the metalliferous deposits along metallogenic provinces (Fontboté 2018). This W to E zonation reflects the
186 constraining character of the source regions and the decrease in the role of subduction-related processes evidenced
187 by difference in granitoid type and series (Mlynarczyk and Williams-Jones 2005).

188 **Geological setting of the Bolivian Tin Belt**

189 The deposits selected for this study are distributed along the Bolivian segment of the Bolivian tin belt. The
190 Bolivian tin belt is restricted to the Eastern Cordillera and stretches for about 900 km from ~150 km NNW of Lake
191 Titicaca in Peru (e.g., the San Rafael world-class Sn deposit) through Bolivia to NW Argentina (e.g., the Pirquitas

192 Ag-Zn-Pb-Sn deposit; Fig. 1A). It has an arc shape with contrasting orientations in its northern half (running NW-
193 SE) and southern half (running N-S), both segments connecting in the so-called "elbow of the Andes", Bolivian
194 orocline or Arica deflection (Ahlfeld 1967; Maffione et al. 2009).

195 The Bolivian tin belt is genetically connected to two major periods of magmatism related to the Andean orogeny:
196 the first is linked to intrusions of granitic plutons of Triassic to Jurassic ages and the second is related to plutonic,
197 sub-volcanic and volcanic eruptive complexes of Oligocene to Miocene ages (Turneaure 1971; Sillitoe et al. 1975;
198 Evernden et al. 1977; Lancelot et al. 1978; Grant et al. 1979; Clark et al., 1983, 1990, 2000; McBride et al. 1983;
199 Kontak et al. 1987, 1990; Mlynarczyk and Williams-Jones 2005; Maffione et al. 2009; Mišković et al. 2009;
200 Reitsma 2012; Betkowski et al. 2017; Cordani et al. 2019). The Triassic granite intrusions were interpreted as
201 typical of rift-related magmatism in a back-arc setting (McBride et al. 1983; Kontak et al. 1984, 1990; Lehmann et
202 al. 1990; Miskovic et al. 2009; Reitsma 2012). The now-inverted rift system had an axis coinciding with the axis
203 of the current Eastern Cordillera (Sempere et al. 2002). In the Cordillera Real, at the core of the Eastern Cordillera
204 and the northern portion of the Bolivian tin belt, the oldest dated granitoids belong the Huato, Illampu, Yani,
205 Huayna Potosí, Zongo and Taquesi plutons (ca. 280-200 Ma) and the youngest, to the Illimani, Quimsa Cruz and
206 Santa Vera Cruz plutons (ca. 26-23 Ma; Fig. 1A). In the Peruvian segment of the Bolivian tin belt, known as the
207 Cordillera de Carabaya, the oldest granitoids (San Gabán, Coasa, Limbani and Aricoma plutons; Fig. 1A) have a
208 Triassic age (ca. 240-190 Ma). At the northern end of the Bolivian tin belt, the Nevado de Allincapac peralkaline
209 volcano-plutonic complex comprises gabbros, diorites and nepheline syenites dated between 175 and 181 Ma
210 (Stewart et al. 1974; Kontak et al. 1990), and the youngest dated granitoids (San Rafael and Santo Domingo
211 plutons) and their volcaniclastic equivalents of the Picotani Group (Sandeman et al. 1997) are of Late Oligocene
212 age. South of the Cordillera Real, caldera complexes and huge volumes of Late Pliocene and Miocene (and up to
213 recent) ignimbrite deposits of dacite and rhyolite composition formed as a result of changes in mantle melt
214 productivity induced by the south-migrating subduction of the aseismic Juan Fernández Ridge and sporadic lower-
215 crust and subcontinental lithospheric mantle delamination (de Silva and Kay 2018 and references therein).

216 Compared to the Chilean and NW-Argentinian part of the Central Andes, rock suites in the Bolivian tin belt
217 present higher abundance of Sn and sustained enrichment trends controlled by fractional crystallization (Lehmann
218 et al. 1990). Despite being distinctly enriched in Sn, igneous rocks of Miocene porphyry systems in the Bolivian
219 tin belt show concentrations of Ta, Zr and TiO_2 comparable to average upper crust and overall moderately
220 fractionated rhyodacite and dacite bulk composition. In stark contrast, quartz-hosted melt inclusions in these rocks

yield highly fractionated rhyolitic compositions and enrichment in incompatible elements such as Ta, B, Cs, Li and Sn at concentrations comparable to those of tin granite systems worldwide (Dietrich et al. 2000; Lehmann et al. 2000). These authors propose that highly fractionated melts, chemically linked to the tin mineralization, mixed with primitive melts within magma chambers previous to shallow emplacement as sub-volcanic intrusions or volcanic eruption. Mio-Pliocene lithophile-rich obsidian glasses in felsic peraluminous tuffs in the Macusani area, in the Carabaya Cordillera in SE Peru, are representative of these highly evolved igneous rocks portions (Pichavant et al. 1987, 1988a,b; Cheilletz et al. 1990; Poupeau et al. 1993; Sandeman et al. 1997; Nupen 2019). Subsequent hydrothermal redistribution of Sn from igneous rocks magmatically enriched in this element led to enhancement of Sn concentrations. In this model, Sn inheritance from source and host rocks is discarded. Nevertheless, source sedimentary sequences played an important role in magma evolution by providing B and C_{org} that depressed the solidus temperature of fractionating melts and induced a low oxidation state necessary for magmatic enrichment and hydrothermal redistribution of tin, respectively (Lehmann et al. 1990, 2000; Dietrich et al. 2000). In addition, the high concentration of B and other volatile elements in melt inclusions in tin porphyries from the Bolivian tin belt led Lehmann et al. (2000) to conclude that the most likely crustal source was the Lower Paleozoic meta-sedimentary sequences.

Mineral deposits from the northern and southern halves of the Bolivian tin belt show contrasting ages and levels of emplacement (Kelly and Turneaure 1970; Sillitoe et al. 1975; Clark et al. 1976; Lehmann et al. 1990; Heuschmidt et al. 2002; Kontak and Clark 2002; Slater et al. 2020). In the northernmost part, the ore deposits are mainly of Sn-W vein- and “manto”- (stratabound mineralization) type related to batholiths of Triassic and Oligocene age, whilst in the southernmost segment of the belt, mineralization is Miocene, usually shallower and appears as Sn, Sn-W and Sn-polymetallic veins formed in the epithermal and xenothermal environments (Fig. 1). The mineralized stocks and adjacent wall rocks usually present vertically and laterally zoned hydrothermal alteration, with abundant quartz - tourmaline - muscovite assemblages at high-temperature mineralization centers grading outward to phyllic, propylitic and, occasionally, silicified, advanced argillic lithocaps (Sillitoe et al. 1975, 1998; Harlaux et al. 2020; Lehmann et al. 2000). Lithocaps are only found in the southern part of the Bolivian tin belt, where volcanic domes genetically linked to the mineralization are only shallowly eroded (Sillitoe et al. 1998). Detailed descriptions of deposits from the Bolivian tin belt are given by Ahlfeld and Schneider-Scherbina (1964), Kelly and Turneaure (1970), Heuschmidt et al. (2002) and Arce-Burgoa (2009).

Methodology

Studied samples and their localities

The studied cassiterite crystals belong to nine ore deposits/districts distributed along the Bolivian segment of the Bolivian tin belt (Fig. 1A-B).

Milluni-Kellhuani district

The Milluni-Kellhuani Zn-Cu-W-Bi district is located in the northernmost part of the La Paz department and sits at the northern part of the Cordillera Real, ~ 5 km south of the Triassic Huayna-Potosí granite (Gillis et al. 2006; Cordani et al. 2019). Vein and stratabound mineralization are hosted in Silurian quartzites of the Catavi Formation. Mineralization consists primarily of early quartz, tourmaline and cassiterite (Sn-W stage) and later sulfides such as chalcopyrite, sphalerite, pyrrhotite and pyrite (sulfide stage; Lehmann et al. 1985). Fluid inclusions in cassiterite from the Milluni mine yielded trapping temperatures of 410-500ºC (corrected for depositional pressures of 0.5-1 kbar) and salinities of 5-25 wt% NaCl equiv. (Kelly and Turneaure 1970).

In the central part of the district, the Chacaltaya granite porphyry stock, which shows extreme hydrothermal alteration (greisenization), intruded the Paleozoic metasedimentary rocks (Lehmann 1985). Mineralization in the greisen is mostly composed of cassiterite accompanied by fine- and medium-grained quartz, muscovite, tourmaline, fluorite and siderite. K-Ar dating of greisen muscovite yielded a date of 210 ± 6 Ma (McBride et al. 1983).

The analyzed cassiterite crystals belong to two samples of quartz-cassiterite veins from the Kellhuani deposit (Kell A and Kell B) about 3 km east of the granite porphyry. Crystals are dark red in color, euhedral and subhedral and have sizes typically larger than 500 μm and exceptionally up to 5 mm across (Fig. 2A); some contain inclusions of pyrrhotite and are intergrown with quartz and tourmaline.

Viloco – Rosario de Araca district

The Viloco – Rosario de Araca district is located in the La Paz department, 70 km SE of La Paz, on the southwestern flank of the Quimsa Cruz Cordillera in the southern segment of the Cordillera Real. NE-trending peribatholitic veins are hosted by Ordovician quartzites of the Amutara Formation close to their contact with the Oligocene Quimsa Cruz granodiorite and porphyritic monzogranite batholith (Everden et al. 1977; Gillis et al.

2006; Artiaga et al. 2013). K-Ar dating of igneous biotite and muscovite from the Quimsa Cruz batholith yielded dates between 23 and 26 Ma (Ahlfeld and Branisa 1960; Cordani 1967 in Clark and Farrar 1973; Evernden et al. 1977; McBride et al. 1983; Gillis et al. 2006). U-Pb zircon dates in the Quimsa Cruz batholith at Mina Argentina and Mina Viloco are 25.65 ± 0.41 and 26.02 ± 0.41 Ma, respectively (Gillis et al. 2006).

Vein mineralogy comprises early high-temperature cassiterite, wolframite, löllingite and pyrrhotite associated with quartz-tourmaline gangue and a second lower temperature sulfide stage with arsenopyrite, sphalerite, galena, chalcopyrite and stannite in association with sulfosalts and carbonate gangue minerals (Sugaki et al. 1985; Artiaga et al. 2013). Fluid inclusions in cassiterite crystals from the Araca deposit yielded salinities of 23-35 wt% NaCl equiv. and homogenization temperatures (T_h) of 340-489ºC (Kelly and Turneaure 1970). Cassiterite from this district is world renowned for its large, highly lustrous, black to caramel-color, twinned and euhedral crystals of gem quality.

Cassiterite crystals studied from this district belong to seven samples collected from the Viloco deposit (Vil 1-540d, Vil-2-sn-a, Vil2-453-2b, Vil2-453-2c, Vil4-453-2b, Vil41-xa and Vil5e). In the studied samples, cassiterite is the dominant phase and appears as dark euhedral and subhedral fractured crystals more than 500 µm and up to 5 cm across (Fig. 2B). Twining is a common feature of most cassiterite grains. Crystals present sharp edges in contact with an assemblage of quartz and corroded pyrite-marcasite after pyrrhotite (Fig. 2C). Small sulfide veinlets, less than 200 µm in width and containing chalcopyrite and arsenopyrite, cut cassiterite grains.

San José – Itos district (Oruro city)

The San José and Itos mines are located on the western side of the city of Oruro, 200 km SE of La Paz, and sit close to the contact between the Altiplano and the Eastern Cordillera. Metallic mineralization is genetically associated to a Miocene dome and volcanic complex intruding into and extruding over Paleozoic shales and sandstones (Chace 1948a,b; Redwood and Macintyre 1989; Sugaki et al. 2003). K-Ar dating of biotite, sericite and K-feldspar in rhyodacite domes yielded dates between 15 and 19 Ma (McBride et al. 1983; Redwood and Macintyre 1989). Mineralization appears as Ag-Sn-rich veins and disseminations hosted by domes of 16.1 Ma (Redwood and Macintyre 1989) and hydrothermal breccias of the homonymous San José and Itos stocks (Sillitoe et al. 1975; Sugaki et al. 1990).

Mineralization occurred in three stages. The first stage is Sn-rich and composed of euhedral quartz, As-rich pyrite, cassiterite and arsenopyrite. The second stage is sulfosalt-rich and comprises franckeite and cylindrite coatings

over previous assemblages. The third stage is composed of sphalerite and stannite-group minerals partially replaced by franckeite and Ag-rich sulfosalts (stephanite, andorite), acanthite and galena as open-space infilling and associated to kaolinite, dickite and alunite (Sillitoe et al. 1975; Pastor et al. 2015). Bismuth-rich andorite and ramdohrite and Sb-rich bismuthinite are also found in the San José mine (Keutsch and De Brodtkorb 2008). Fluid inclusions in cassiterite from the Oruro district yielded T_h of 389-474ºC and salinities of 8.9 to 26.3 wt% NaCl equiv. (Kelly and Turneaure 1970).

Here studied cassiterite crystals are from six samples collected from the Itos (It-180b, It-250b and It-250d) and San José (1233, 1241 and 1433) mines. Cassiterite forms massive aggregates of crystals ranging in size from a few tens of microns up to 500 µm. Most aggregates are highly corroded and show abundant porosity that draws secondary spongy textures (Fig. 2D). Cassiterite aggregates occur usually assembled with quartz, pyrite-marcasite, arsenopyrite and late sulfosalts such as jamesonite that replaced the previous sulfide assemblage. Locally, euhedral cassiterite crystals are intergrown with quartz (Fig. 2E).

Poopó district

The Poopó deposit is located 48 km S of Oruro and 240 km SE of La Paz, near the border between the Altiplano and the Eastern Cordillera delineated by the NNW–SSE striking Poopó regional fault. The Sn-Ag low-sulfidation epithermal mineralization consists of a vein system extending along the N-S striking Poopó-Uyuni fault system. Veins are hosted by Silurian black shales and sandstones of the Llallagua, Uncía and Belén Formations that were intruded by Miocene dacite porphyry stocks and covered by associated ignimbrite deposits (Heuschmidt et al. 2002). Conspicuous cataclastic textures and occurrence of several stages of breccia cementation by hydrothermal minerals suggest that ore mineralization was coeval with the tectonic activity of the Poopó-Uyuni fault (Torres et al. 2019).

The mineralogy of the deposit consists primarily of quartz, sulfides (sphalerite, wurtzite, pyrite and marcasite), cassiterite, which locally amounts to about 10% of the vein assemblage, and a plethora of Ag-Pb-Cu sulfosalts (Torres et al. 2019). Cassiterite crystallized at two stages during the formation of the deposit: the first one, with quartz and sphalerite-pyrite (Zn-Sn stage) and the second one, along with tin sulfides and sulfosalts (Sn stage).

Analyzed cassiterite grains are from sample Poo-St-1c, which was collected from the Santo Toribio vein system, and belong to the first generation crystallized during the Zn-Sn stage. In the studied samples, cassiterite appears as small aggregates of crystals with sizes between a few tens of microns and 1 mm. Cassiterite is often intergrown

with pyrrhotite that has been pervasively replaced by an assemblage of pyrite and marcasite along with siderite (Fig. 2F).

Huanuni district

The Huanuni Sn-W-Pb-Ag-Zn world-class district, located in the homonymous city in the Oruro department, 275 km SE of La Paz, is the largest tin producer in Bolivia and in 2018 its production accounted for over half the total tin production of the country. This deposit is considered to be mesothermal or xenothermal (Cacho et al. 2019). Mineralization is mostly hosted by Silurian quartzites, shales and siltstones of the Llallagua, Uncía and Cancañiri Formations, which are discordantly overlain by pyroclastic series of the Miocene Morococala Formation (Koeppen et al. 1987). Paleozoic rocks were intruded by Miocene porphyric dikes peripheral to the mineralized area, which are thought to be genetically connected to the hydrothermal mineralization (Redwood 1993; Heuschmidt et al. 2002; Cacho et al. 2019). Cassiterite-rich veins are restricted to the central area of the deposit, in the Pozokoni hill, and tin concentration decreases towards the periphery in the Zn-Pb-Ag La Suerte and Bonanza mines, which are rich in sphalerite, galena and sulfosalts.

Hypogene mineralization in the Pozokoni area comprises three stages. The first stage consists of quartz, base-metal sulfides and cassiterite. The second stage records abundant crystallization of schorl and, akin the first stage, is also rich in base-metal sulfides as well as Co-Ni minerals, late chamosite and siderite followed by native bismuth, wolframite and cassiterite. The third stage is characterized by stannite and sphalerite. There was, in addition, ample crystallization of supergene minerals dominated by phosphates, sulfates and carbonates rich in Fe, Cu and Pb (Cacho et al. 2019). Fluid inclusions in quartz from quartz-cassiterite veins yielded T_h up to 425ºC and salinities up to 26 wt% NaCl equiv. (Sugaki et al. 1988b; Müller et al. 2001; Arce-Burgoa 2009).

Studied cassiterite grains belong to six samples collected from the Pozokoni hill mine area (Hua240, Hua240-1a, Hua240-1b, Hua240-3c, Hua-MU-7b and Hua-MU-8). Cassiterite is the most abundant phase in the studied samples and appears as large (>1 to 5 mm) subhedral and anhedral crystals often forming centimetric aggregates with abundant porosity (Fig. 2G). Twinning is a common feature of Huanuni cassiterite. The edges of the cassiterite crystals are usually sharp in contact with quartz and irregular in contact with marcasite-pyrite and pyrrhotite. In addition, cassiterite crystals are wrapped by stannite, which also lines fractures and voids within cassiterite.

Llallagua district

The Llallagua district is located next to the homonymous city, 300 km SE of La Paz and 80 km SE of Oruro. It is one of the world's largest porphyry-tin deposits with a historical production exceeding 500,000 t of tin (Ahlfeld and Schneider-Scherbina 1964). The deposit lies in the hydrothermally altered La Salvadora stock, which is composed mostly of porphyry breccias. The stock is pervasively altered to tourmaline in the central areas and at depth grading upwards and outwards to intense sericitization and finally to chloritization and argilitization (Betkowski et al. 2017). The stock is cut by igneous and hydrothermal breccias. Tin mineralization appears disseminated and in quartz-cassiterite-sulfide veins restricted to early, high-temperature stages (Kelly and Turneaure 1970). In veins, cassiterite is assembled with pyrrhotite and apatite (Turneaure 1935; Gordon 1944; Kempe et al. 2008). Fluid inclusions in cassiterite and quartz yielded salinities up to 8.2 and 26 wt% NaCl equiv., respectively, and T_h up to 593ºC (Kelly and Turneaure 1970).

Reported radiometric dates are 43.8 Ma (Sm-Nd fluorapatite age; Rakovan et al. 1997), 42.4 Ma (Pb-Pb zircon evaporation geochronology; Kempe et al. 2008), 23.4 and 19.0 Ma (U-Pb monazite; Kempe et al. 2008 - SHRIMP and Kohn and Vervoort 2008 - LA-ICP-MS, respectively). Recent U-Pb cassiterite dating by Neymark et al. (2018) yielded a date of 20.0 ± 2.5 Ma.

Analyzed cassiterite grains are from sample LL-4, which was collected from the Siglo XX mine. In the studied sample, cassiterite occurs as anhedral, fractured and corroded relatively large crystals, with sizes in the range between 200 and 500 µm, often showing simple twinning (Fig. 2H). Cassiterite grains are intergrown with quartz, tourmaline and small pyrite crystals with cores replaced by marcasite.

Colquechaca deposit

The Ag-(Zn-Sn-Pb) Colquechaca deposit is located in the Hermoso hill in Colquechaca, northern Potosí department, 465 km SW of La Paz and 96 km N of Potosí. Mineralized veins are hosted by the Miocene Colquechaca volcanic complex in which a stratovolcano of andesitic to dacitic composition was intruded by a series of porphyritic rhyodacitic and quartz-latite domes. The volcanic complex is emplaced over metasedimentary Ordovician (Amutara Formation) and Silurian (Cancañiri and Uncía Formations) series and the discordantly overlying Jurassic (Ravelo Formation), Jurassic-Cretaceous (Kondo and Kosmina Formations) and Cretaceous (Tarapaya Formation) sedimentary series (Martínez and Vargas 1990; Claure et al. 1996; Díaz 1997; Heuschmidt

et al. 2002). K-Ar dating of igneous biotite, K-feldspar and plagioclase yielded dates in the range between 19.8 and 22.6 Ma (Ahlfeld and Schneider-Scherbina 1964; Thormann 1966; Evernden et al. 1977; Grant et al. 1979).

Xenothermal vein mineralization hosts a cassiterite- and stannite-rich zone along with tourmalinization in the innermost part of the deposit, which grades outwards to a sulfide- and Ag-sulfosalt-rich domain with phyllic alteration (Grant et al. 1979; Heuschmidt et al. 2002).

Analyzed cassiterite grains are from two samples collected from the Hilarion vein in the Cerro Ánimas area (Colq6a and 1353). Cassiterite grains form mostly anhedral crystals of approximately 400 µm across (Fig. 2I). The edges of these crystals are sharp in contact with quartz and tourmaline and more irregular in contact with sulfides (pyrite, sphalerite and galena). Local leather-shaped radial aggregates of cassiterite appear in contact with most massive, anhedral cassiterite crystals (Fig. 2J).

Huari Huari district

The Huari Huari xenothermal vein deposit is located 25 km NE of Potosí in the Potosí department, 400 km SW of La Paz. Vein and much restricted stratabound metallic mineralizations are hosted by slates and quartzites of the Ordovician San Benito and Silurian Cancañiri and Uncía Formations, which are unconformably overlain by Cretaceous sandstones of the La Puerta Formation. The sedimentary sequence was intruded by small dacite domes and stocks of alleged Miocene age (Sugaki et al. 1983; Torró et al. 2019a).

Polymetallic veins are mostly of the fissure-filling type and NNE-oriented. Vein mineralogy consists primarily of an early assemblage of quartz, cassiterite and pyrrhotite followed by an assemblage dominated by base-metal sulfides (sphalerite, galena) and pyrite and a final stage dominated by Ag-Pb sulfosalts (Torró et al. 2019a).

Analyzed cassiterite grains belong to three samples collected from the Antón Bravo vein (2018hh15, 2018hh2b and 2018hh3a). In the studied samples, cassiterite is rare and mostly of the "*needle tin"* variety (i.e., small micrometric acicular crystals) forming radial aggregates up to 500 µm in size. Nevertheless, in the deepest parts of the Antón Bravo vein, cassiterite appears as subhedral crystals in assemblage with quartz and a complex paragenesis of sulfides and sulfosalts (Fig. 2K).

409 ***Ánimas – Chocaya – Siete Suyos district***

410 The Ánimas - Chocaya - Siete Suyos district is located about 150 km S of Potosí in the Potosí department, 520 km
411 SW of La Paz. This district sits in the western flank of the Eastern Cordillera, close to the triple junction that is
412 drawn by the Eastern Cordillera, the Western Cordillera and the Altiplano. Mineralization is genetically associated
413 with the Miocene Chocaya volcanic caldera complex, which is 9 km in diameter and conformed of a pile of lava
414 and pyroclastic deposits of dacitic composition intruded by a central dome of the same composition. The volcanic
415 complex is hosted by Ordovician sandstones and slates unconformably overlain by Oligocene-Miocene sandstones
416 and tuffs of the Quehua Formation (Ahlfeld and Schneider-Scherbina 1964; Grant et al. 1979; Arce-Burgoa 2009;
417 Torró et al. 2019b). Reported K-Ar dates in the area are of 13.8 ± 0.2 Ma (unweighted mean value) for biotite from
418 unaltered volcanic rocks, and of 12.5 ± 0.2 Ma for a sericitized sample (whole-rock age; Grant et al. 1979).

419 Mineralization in the district occurs as banded and massive oxide and sulfide ore vein infillings (Sugaki et al.
420 1983). Torró et al. (2019b) determined a three-stage paragenetic sequence including an early low-sulfidation stage
421 dominated by cassiterite, pyrrhotite, arsenopyrite and high-Fe sphalerite, a second intermediate-sulfidation stage
422 dominated by pyrite, marcasite, sphalerite and stannite and a late intermediate-sulfidation stage dominated by
423 galena and Ag-Pb-Sn sulfosalts. Cassiterite is much abundant in the Siete Suyos deposit and less common in the
424 Ánimas deposit. In the Chocaya deposit, cassiterite is virtually absent (Torró et al. 2019b).

425 Analyzed cassiterite grains are from the 10 vein in the Siete Suyos mine (2018-7S2 and 1380) and from the
426 Colorada vein in the Ánimas mine (2018-An12 and Ani5c). The studied grains are subhedral and anhedral and
427 range in size from 100 to 600 µm. Often, small crystals of cassiterite form aggregates up to 1 mm across. These
428 aggregates are intergrown with quartz, sulfides and sulfosalts in hexagonal arrangements (Fig. 2L) after hexagonal
429 pyrrhotite (see Torró et al. 2019b).

430 **Analytical methods**

431 A total of 32 thick sections belonging to nine deposits from the Bolivian tin belt were selected: two for Kellhuani,
432 seven for Viloco, six for San José-Itos (Oruro), one for Poopó, six for Huanuni, one for Llallagua, two for
433 Colquechaca, three for Huari Huari and five for Ánimas - Chocaya - Siete Suyos.

Petrography (optical microscope, SEM and SEM-CL)

Mineralogy and textures in thick polished sections were studied by optical microscopy using reflected light in order to select the optimal cassiterite specimens for subsequent geochemical analysis. A selection of the polished sections was also examined with an environmental scanning electron microscope (SEM) Quanta 200 FEI, an XTE 325/D8395 (Thermo Fisher Scientific, Waltham, MA, USA) equipped with an INCA Energy 250 EDS microanalysis system at the Centres Científics i Tecnològics of the University of Barcelona (CCiT-UB). Operating conditions were 20 keV accelerating voltage and 5 nA in backscattered electron (BSE) mode.

Electron probe microanalysis (EPMA)

A total of 268 analyses of cassiterite (major and minor elements) were carried out using a five-channel JEOL JXA-8230 electron probe microanalyzer (EPMA; Jeol Ltd., Tokyo, Japan) at the CCiT-UB, operated at 20 kV acceleration voltage, 20 nA beam current, and with a beam diameter of 5 µm. Analytical standards and lines used for analyses were: ZrO_2 (Zr, Lα), Nb_2O_5 (Nb, Lα), SnO_2 (cassiterite, Lα), FeO (Fe, Kα), Ta_2O_5 (Ta, Lα), MnO (rhodonite, Kα), TiO_2 (rutile, Kα). The EPMA data are reported in Supplementary Table S1.

Laser ablation – inductively coupled plasma – sector field – mass spectrometry (LA-ICP-SF-MS)

A total of 330 analyses of cassiterite trace element concentrations and U-Pb isotopic compositions were carried out at ETH Zürich, Switzerland, by laser ablation – inductively coupled plasma – sector field – mass spectrometry (LA-ICP-SF-MS) using a RESOlution S-155 (ASI/Applied Spectra) 193 nm ArF excimer laser system attached to an Element XR (Thermo) sector-field ICP-MS. We have used a laser repetition rate of 3 Hz, a spot diameter of 43 µm and a laser energy density on sample of about 3.5 $J \cdot cm^{-2}$. The sample surface was cleaned before each analysis by three pre-ablation pulses. Ablation was performed in a dual-volume, fast-washout S-155 ablation cell (Laurin Technic) fluxed with carrier gas consisting of about 0.5 $L \cdot min^{-1}$ He and make-up gas consisting of about 1 $L \cdot min^{-1}$ Ar and 2 $mL \cdot min^{-1}$ N_2. The ablated aerosol was homogenized via flushing through a squid device before being introduced in the plasma.

The ICP-MS instrument is equipped with a high capacity (80 $m^3 \cdot h^{-1}$) interface pump to achieve, in combination with jet sampler and normal H-skimmer cones, a detection efficiency (based on U in NIST SRM612 glass) in the range of 2% (Guillong et al. 2020). The instrument was optimized for maximum sensitivity on the entire mass range while keeping the production of oxides low ($^{248}ThO^+/^{232}Th^+ \leq 0.15\%$) and the U/Th ratio at about 1 (on

NIST SRM612 glass). The list of analyzed isotopes and corresponding dwell times is provided in Supplementary Table S2. A total of 40 mass scans (~1.04 s sweep time each) were acquired over 40 s measurement (20 s of background measurement followed by 20 s of sample ablation).

For trace element quantification, the resulting intensities were subsequently processed offline with the standalone version 1.3.2 of the SILLS program (Guillong et al. 2008). The USGS GSD-1G glass (Guillong et al. 2005) was used as the primary reference material for trace element quantification and instrumental drift correction using conventional standard-sample bracketing. The Fe concentrations obtained by electron microprobe were used as internal standards for relative sensitivity corrections. The analyzed In intensities on masses 113 and 115 were corrected for interferences by subtracting the contribution of ^{113}Cd and ^{115}Sn, respectively, based on the measured ^{111}Cd and ^{118}Sn intensities and using natural isotope ratios for Cd and Sn recommended by IUPAC. Because of the very high ^{118}Sn signal in cassiterite (>5,109 cps) and resulting elevated gas blanks on masses 115 and 118, the extent of the correction is much higher in the case of ^{115}In than in the case of ^{113}In, especially since the analyzed cassiterite crystals all show very low Cd concentrations (<1 ppm). Therefore, we only considered the concentrations based on the interference-corrected ^{113}In intensities. The data are reported in Supplementary Table S3. The analytical reproducibility and accuracy were checked by repeated measurements of the homogeneous NIST SRM610 glass (Jochum et al. 2011) reference material. Reproducibility ranges from 10 to 15% (2σ) relative for most elements. The quoted uncertainties for each individual analysis correspond to the internal (2σ) statistical error and analytical reproducibility propagated by quadratic addition. The results are accurate within these calculated uncertainties (Supplementary Table S3).

For U-Pb dating, the measured intensities were subsequently processed offline with the Igor Pro Iolite v2.5 software (Hellstrom et al. 2008), using the VizualAge data reduction scheme (Petrus and Kamber 2012). Background-subtracted intensities were used to calculate isotope ratios, which were corrected for laser-induced Pb/U fractionation (after Paton et al. 2010), instrumental mass discrimination and drift by conventional standard-sample bracketing, against rutile reference material R10 (using isotope ratios from Luvizotto et al. 2009). No common Pb correction was carried out. U-Pb age calculations and data plotting were performed using the IsoplotR toolkit (Vermeesch 2018). The lack of matrix-matched primary reference material most certainly makes the obtained dates inaccurate. Nevertheless, in another session using exactly the same analytical parameters as here (including the use of R10 rutile as primary reference material), we have measured three cassiterite samples of known age from the San Rafael granite, Peru (ca. 24 Ma, samples and unpublished dates courtesy of K.

Kouzmanov, University of Geneva, 2020) and obtained a systematic offset of ca. 8% relative on lower intercept dates. This offset is in any case smaller than the relative uncertainty obtained on the cassiterite dates obtained here (13-53% relative), except for samples Kell-A and Kell-B (3-6% relative). For these two samples, a relative uncertainty of 8% was therefore propagated in the uncertainty of the dates by quadratic addition to account for the matrix effects. The data from unknowns and rutile reference material are provided in Supplementary Table S4.

Results

Major- and minor-element composition

The EPMA data of cassiterite grains from the studied Bolivian deposits show a generally restricted range in composition, with SnO_2 > 97.7 wt%. Of the other elements, only Fe yields concentrations that are generally above its lower limit of detection (L.O.D.) with maximum concentrations of 2.34 wt%. Iron is particularly high in cassiterite from the Colquechaca deposit, with concentrations systematically higher than 0.5 wt%. The rest of the elements yields values mostly below the respective L.O.D. with some anomalous values for TiO_2 (up to 0.92 wt% in a sample from Kellhuani) and Nb_2O_5 (up to 0.25 wt% in samples from Viloco and Huanuni).

Trace-element composition

Significant effort was made to report only the concentration of elements whose variations respond to solid solutions and not to mixed mineral analyses by analyzing mineral volumes free of obvious inclusions and by selecting only stable signal intervals in LA-ICP-MS spectra (Supplementary Fig. S1). A complete set of box plots showing the concentration of all elements analyzed by LA-ICP-MS is available in Supplementary Figure S2, and a selection of them is shown in Fig. 3. Concentration values will be hereinafter reported as the interquartile range (IQR) unless otherwise specified.

Cassiterite from the Bolivian tin belt shows a relatively wide trace element compositional spectrum, mainly subordinated to W (1987-53.7 ppm) and Ti (918-27.8 ppm) contents. The concentration of high-field-strength elements (HFSE) is relatively low, including Zr (17.0-0.528 ppm), Hf (0.293-0.0455 ppm), Nb (4.84-0.037 ppm) and Ta (0.0924-0.0126 ppm). The highest concentrations of Nb and Ta are found in cassiterite samples from the Kellhuani (60.8-2.26 ppm Nb and 0.639-0.0403 ppm Ta), Llallagua (18.5-0.989 ppm Nb and 0.185-0.0143 ppm Ta) and Viloco (6.19-0.0515 ppm Nb and 0.135-0.0138 ppm Ta) deposits, and the lowest, in cassiterite samples from the Poopó (0.027-0.0126 ppm Nb and 0.0196-0.0133 ppm Ta) and Ánimas - Chocaya - Siete Suyos (0.059-

517 0.00971 ppm Nb and 0.0165-0.00873 ppm Ta) deposits. Manganese concentrations (9.36-1.61 ppm) are
518 consistently lower than Fe concentrations. Maximum Mn concentrations are recorded in samples from the
519 Colquechaca (40.4-3.28 ppm) and Poopó (17.5-8.38 ppm) deposits, and the lowest concentrations, in samples from
520 the Llallagua deposit (<L.O.D.). Most analyzed cassiterite samples from the Bolivian tin belt yield
521 (Fe+Mn)/(Nb+Ta) >> 1 at relatively constant Mn (and Fe+Mn) and variable Nb+Ta (Fig. 4A-B; see also
522 Supplementary Fig. S3). In the Nb vs Ta plot (Fig. 4C), cassiterite samples from the Bolivian tin belt plot mostly
523 around the Nb:Ta = 2:1 ratio line, Nb concentrations being by up to four orders of magnitude higher than Ta
524 concentrations.

525 Concentrations of Zr and Hf are highest in samples from the Kellhuani (28.5-3.24 ppm Nb and 0.965-0.141 ppm
526 Ta), Huanuni (17.5-1.89 ppm Nb and 0.432-0.0731 ppm Ta) and Llallagua (16.5-3.92 ppm Nb and 0.387-0.0955
527 ppm Ta) deposits, and lowest in samples from the Ánimas - Chocaya - Siete Suyos (0.059-0.00971 ppm Nb and
528 0.0165-0.00873 ppm Ta) and Poopó (0.027-0.0126 ppm Nb and 0.0196-0.0133 ppm Ta) deposits. The
529 concentration of both elements yields a relatively good positive correlation mostly at Zr/Hf > 1, Zr concentrations
530 being by up to one order of magnitude higher than Hf concentrations (Fig. 4D). Concentrations of Ti are highest in
531 cassiterite samples from Kellhuani (3065-561 ppm), Huari Huari (1391-383 ppm) and Llallagua (1303-382 ppm)
532 and lowest in samples from Ánimas - Chocaya - Siete Suyos (19.1-4.65 ppm) and Poopó (4.38-2.02 ppm). There is
533 a fairly positive correlation between Ti and Zr at Ti/Zr > 1, similar to most cassiterite worldwide (Fig. 4E). In
534 contrast, Ti does not show clear correlation with U, and Ti/U ratios are normally higher than 1, with a composition
535 similar to global cassiterite in terms of both elements (Fig. 4F). Titanium shows fairly positive correlation with Sc
536 for most samples plotting between the lines defined by Sc:Ti 1:1 and 1:2 ratios in Fig. 4G. Nevertheless, cassiterite
537 compositions for some of the studied deposits align preferably along one or the other, with most samples from the
538 Kellhuani and Viloco deposits lying along the Sc:Ti = 1:2 ratio line and most samples from the Ánimas - Chocaya
539 - Siete Suyos and Poopó deposits lying around the 1:1 ratio line. Finally, there is a strong positive correlation
540 between V and Sc (Fig. 4H).

541 As for the concentrations of critical metals others than the aforementioned ones (European Commission 2017), In
542 (96.9-9.78 ppm), Ga (92.1-3.03 ppm) and Ge (3.92-0.776 ppm) vary by orders of magnitude in crystals from
543 individual deposits/districts and from deposit to deposit. Gallium and In are distinctively concentrated in cassiterite
544 from the Oruro (801-31.8 ppm In and 377-71 ppm Ga), Huari Huari (889-96.9 ppm In and 438-53.5 ppm Ga) and
545 Ánimas - Chocaya - Siete Suyos (582-174 ppm In and 292-53.1 ppm Ga) deposits. Gallium is also relatively high

546 in the Colquechaca deposit (438-53.5 ppm). The concentrations of In and Ga are consistently very low in the
547 Viloco (63.4-10.0 ppm In and 5.43-1.59 ppm Ga), Kellhuani (30.9-2.15 ppm In and 3.11-0.932 ppm Ga),
548 Llallagua (25-6.5 ppm In and 53.1-23.0 ppm Ga) and Poopó (4.7-3 ppm In and 43.3-27.3 ppm Ga; Fig. 3)
549 deposits.

550 REE values show a relative wide dispersion in grains analyzed within individual deposits/districts (Figs. 3 and 5,
551 Table 1). Cassiterite samples from Kellhuani (IQR[∑REE] = 6.18-2.19 ppm) yield the highest REE
552 concentrations, and samples from the Ánimas - Chocaya - Siete Suyos district (IQR[∑REE] = 2.12-1.44 ppm), the
553 lowest REE concentrations. In chondrite-normalized (CN) spider plots (Fig. 5), studied cassiterite grains show
554 rather parallel patterns with irregular tetrad distribution, general negative Ce and positive Gd and Tb anomalies
555 and enrichment in MREE relative to LREE and HREE ($[\sum LREE/\sum MREE]_{CN}$ between 0.4 and 0.3,
556 $[\sum LREE/\sum HREE]_{CN}$ between 1.6 and 0.6, and $[\sum MREE/\sum HREE]_{CN}$ between 4.5 and 1.7).

557 **U-Pb cassiterite geochronology**

558 U-Pb isotopic analyses of cassiterite grains from the Kellhuani, Viloco, Huanuni and Llallagua deposits are
559 presented in Supplementary Table S4 and illustrated in Fig. 6. Spot analyses from the four deposits form Tera-
560 Wasserburg (T-W) isochrons defining lower-intercept dates of 218.3 ± 5.5 Ma (Kellhuani), 24.4 ± 0.4 Ma
561 (Viloco), 24.0 ± 2.4 Ma (Huanuni) and 24.0 ± 5.1 Ma (Llallagua); concordant data is absent. U-Pb isotopic
562 analyses on cassiterite grains from the other studied Bolivian deposits were inconclusive due to too low U contents
563 and/or too high initial Pb.

564 ## Discussion

565 **Timing of Sn mineralization in the Bolivian tin belt**

566 Punctuated magmatism and petrogenetically related hydrothermal tin mineralization in the Bolivian tin belt
567 occurred in the Late Triassic, Late Oligocene and Miocene (Ahfeld 1967; Turneaure 1971; Clark and Farrar 1973;
568 Evernden et al. 1977; Grant et al. 1979; McBride et al. 1983; Clark et al. 1990; Lehmann et al. 1990; Sugaki et al.
569 2003; Gillis et al. 2006; Neymark et al. 2018). Accordingly, the metallogeny of the Bolivian tin belt results from
570 multiple, discrete events that lead to similar anomalous Sn enrichment in a series of mineral deposits of different
571 affiliation within the magmatic-hydrothermal family.

572 To contextualize our U-Pb cassiterite ages in the framework of the magmatic and metallogenic evolution of the
573 Bolivian tin belt, a geochronologic chart with all available radiometric dates (excluding dates related to
574 exhumation - thermochronology oriented studies, e.g., (U-Th-Sm)/He, fission track) has been produced (Fig. 7).
575 For some of the studied deposits (Kellhuani, Viloco and Huanuni), our U-Pb cassiterite dates are the first
576 geochronologic data based on ore minerals rather than hydrothermal and/or magmatic mineral phases. This
577 observation is particularly important in the case of the Milluni – Kellhuani district and other tin deposits in
578 neighboring areas of the Cordillera Real (Fig. 1A). In the Yani, Sorata, Zongo and Huayna Potosí plutons, there is
579 a large dispersion of radiometric dates (mostly K/Ar and Ar/Ar silicate mineral dates; Fig. 7) from Late Triassic
580 (i.e., the accepted age of host rock crystallization, constrained by U-Pb zircon dating) to dates as young as ca. 35
581 Ma. This dispersion in radiometric dates probably represents protracted isotopic resetting during the complex
582 thermal history undergone by these rocks (cf. Farrar et al. 1988; Kontak et al. 1990; Schildgen and Hoke 2018) but
583 also opens the door to overprinting hydrothermal events connected to mineralization.

584 Our U-Pb cassiterite date for Kellhuani (218.3 ± 5.5 Ma) agrees, within the limits of the analytical error, with the
585 K/Ar muscovite date at 210 ± 6 Ma reported by McBride et al. (1983) for the greisen at the Chacaltaya porphyry
586 stock, which is genetically connected to the mineralization in the Milluni-Kellhuani district (Lehmann 1985). In
587 addition, this date agrees with the U-Pb zircon concordia dates of 222.3 ± 2.4 and 220.8 ± 1.9 Ma reported by
588 Cordani et al. (2019) for two granite samples from the neighboring Huayna Potosí pluton.

589 In the Viloco deposit, our U-Pb cassiterite date (24.4 ± 0.4 Ma) agrees, within error, with felsic magmatism in the
590 Tres Cruces batholith dated at ca. 22-26 Ma via K/Ar analysis of igneous biotite and muscovite (Ahlfeld and
591 Branisa 1960; Cordani 1967 in Clark and Farrar 1973; Evernden et al. 1977; McBride et al. 1983; Gillis et al.
592 2006). Gillis et al. (2006) performed U-Pb dating of zircons from the Quimsa Cruz batholith in the Argentina and
593 Viloco mines and obtained dates of 26.2 ± 0.2 and 25.4 ± 0.2 Ma, respectively.

594 As far as we know, there are no geochronological studies in the Huanuni deposit area. The mineralization has been
595 suggested to be of Late Oligocene - Early Miocene age by analogy with other neighboring mining districts (e.g.,
596 San Pablo stock - Japo - Santa Fe, El Poder and Llallagua; Fig. 1A) for which igneous activity connected to tin
597 mineralization has been dated in the range between ca. 25 and 20 Ma (K/Ar mineral and whole rock dates;
598 Everden et al. 1961; Grant et al. 1979; Sugaki et al. 2003). This age bracket encompasses our 24.0 ± 2.4 Ma U-Pb
599 cassiterite date in the Huanuni deposit. The nearby Mororocala ignimbrites (Fig. 1A), in contrast, are much
600 younger according to Ar/Ar dates of ca. 8-6 Ma provided by Koeppen et al. (1987) (see also Morgan et al. 1998).

601 The age of the mineralization in the Llallagua deposit has long been a topic of discussion. Reported radiometric
602 dating includes dates as disparate as 43.8 ± 4.7 Ma (Sm/Nd early fluorapatite vein assemblages, Rakovan et al.
603 1997), 42.2 ± 4 Ma (Pb/Pb evaporation age in zircon; Kempe et al. 2008), 23.4 ± 2.2 and 19.0 ± 1.6 Ma (U-Pb
604 monazite, Kempe et al. 2008; Kohn and Vervoort 2008) and 20.9 ± 0.4 Ma (K/Ar geochronology of the
605 hydrothermally altered porphyry, Grant et al. 1979). U-Pb dating on cassiterite by Neymark et al. (2018) yielded a
606 date of 20.0 ± 2.5 Ma, which overlaps within error with our 24.0 ± 5.1 Ma U/Pb cassiterite date thus constraining
607 the tin mineralization event in this deposit to the Early Miocene.

608 The new geochronologic data presented here, hence, conform to the idea that tin mineralization events in the
609 Bolivian tin belt occurred at least in two separate epochs during the Late Triassic (Norian; Milluni-Kellhuani
610 district) and the Late Oligocene (Chattian) - Early Miocene (Aquitanian; Viloco, Huanuni and Llallagua deposits).
611 Unpublished cassiterite U-Pb analyses in samples from the San Rafael deposit in Peru yield dates of ca. 24 Ma
612 (pers. comm. M. Harlaux), similar to the Viloco, Huanuni and Llallagua deposits. These ages coincide with major
613 episodes of mantle upwelling, decompression melting and basalt production, and related high heat flow into the
614 overlying crust (see above). Unfortunately, U-Pb measurements of cassiterite grains from deposits located in the
615 southernmost part of the Bolivian tin belt were inconclusive, although previous geochronological data would point
616 to younger mineralization ages of ca. 15-13 Ma (Fig. 7; see also Slater et al. 2020 for a discussion on the age of the
617 Pirquitas deposit in Argentina based on field relationships). Progressively younger tin-polymetallic mineralization
618 towards the south of the Bolivian tin belt during the Pliocene and Miocene might be related to the southward
619 passage of the subducting Juan Fernández aseismic ridge and associated migrating magmatic flare-up (de Silva
620 and Kay 2018); the latter might however have resulted from the southward migration of the onset of Late
621 Oligocene–earliest Miocene major mafic magmatism detected by Fornari et al. (2002), possibly as a consequence
622 of the reconstructed migration of this ridge. Separate tectonic events leading to i) crustal melting of volatile-rich,
623 carbonaceous sediments and ii) enhanced magmatic differentiation and sustained heat production enabled by long
624 crustal residence of mantle-derived melts in a thickened crust converged to form one of the largest Sn
625 accumulations on Earth (Dietrich et al. 2000; Lehmann et al. 2000).

626 **Controls on minor- and trace-element variations in cassiterite**

627 Due to the tetragonal structure of cassiterite and according to charge, radii and coordination of ions compared with
628 Sn^{4+} the following elements are considered to be compatible with cassiterite: Al^{3+}, Fe^{3+}, Ga^{3+}, V^{3+}, Cr^{3+}, Sc^{3+}, Sb^{3+},
629 W^{4+}, U^{4+}, Zr^{4+}, Hf^{4+}, Ti^{4+}, Nb^{5+} and Ta^{5+} (Cheng et al. 2019; Mao et al. 2020). Of these elements, the 4+ charged

630 cations (Zr, Hf, Ti, U and W) can directly substitute for Sn^{4+} (without readjustments of charge balance) while
631 coupled substitution mechanisms are required for differently-charged cations (e.g., Fe, Mn, Nb, Ta and In; Cheng
632 et al. 2019).

633 Zirconium and Hf have similar geochemical behavior, so they usually maintain a near chondritic Zr/Hf ratio of 35-
634 40 (Hoskin and Schaltegger 2003). However, in hydrothermal environments and in highly differentiated igneous
635 rocks, deviations from this ratio (i.e., element pair decoupling) can occur (Bau 1996). Processes such as
636 metasomatism, crystal fractionation in the presence of zircon, hydrothermal alteration or preferential mobilization
637 of Zr in B- and F-rich fluids have been proposed to cause fractionation of Zr over Hf (Cheng et al. 2019). The fact
638 that the studied cassiterite samples yielded Zr/Hf up to 90 agrees with the high activity of B and F during the
639 formation of the mineralization along the Bolivian tin belt, as seen in abundant tourmaline plus fluorite.

640 Even though Nb and Ta are considered to have similar geochemical behavior, large variations in their
641 concentration and ratio occur in cassiterite. Cheng et al. (2019) attribute these variations to processes involving
642 element fractionation during mineral growth due to fluid disequilibrium. However, variations in the concentration
643 of Nb and Ta may also be related to the physical-chemical characteristics of the hydrothermal fluids (Zhao et al.
644 2019; Lerouge et al. 2017). Zhang et al. (2017) noted that cassiterite from high-temperature systems related to
645 highly fractionated Li-F granites and pegmatites has high Nb, Ta and Zr contents (with low Zr/Hf ratios) but low
646 Fe and Mn contents, contrary to cassiterite from low-temperature hydrothermal deposits. On the other hand,
647 isomorphous replacement of Sn_3O_6 by $(Fe,Mn)(Nb,Ta)_2O_6$ is typical of cassiterite in hydrothermal cassiterite-
648 quartz veins and greisen deposits (e.g., Möller et al. 1988; Murciego et al. 1997; Abdalla et al. 2008), whereas
649 isomorphic replacement of $3Sn^{4+}$ by $2(Nb,Ta)^{5+} + (Fe,Mn)^{2+}$ is typical of magmatic cassiterite from rare-element
650 granites and pegmatites (e.g., Tindle and Breaks 1998).

651 Cassiterite grains from the Bolivian tin belt are low in Nb+Ta relative to most cassiterite compiled from the
652 literature, particularly to magmatic cassiterite (Fig. 4A-C, Table 2). Iron and Mn concentrations in cassiterite
653 samples from the Bolivian tin belt fit the composition of most cassiterite described in the literature, with the
654 exception of magmatic cassiterite and cassiterite in greisen mineralizations, which are significantly enriched in
655 Mn. In terms of Fe+Mn and Nb+Ta, cassiterite from the Bolivian tin belt shows limited dispersion without any
656 correlation between the concentrations of Fe+Mn and Nb+Ta (Figs. 4A-B); these observations suggest that neither
657 of the aforementioned substitution mechanisms was significant in the composition of the studied grains. Regarding
658 Nb and Ta systematics, the compositions of cassiterite samples from the Bolivian tin belt lie largely along the

659 Nb:Ta = 2:1 ratio line similar to most cassiterite in hydrothermal occurrences worldwide, whereas most magmatic
660 cassiterite and cassiterite from greisen mineralizations lie rather along the 1:1 ratio line (Fig. 4C). Niobium and Ta
661 are enriched in cassiterite grains from the sediment-hosted Kellhuani and Viloco xenothermal deposits, which
662 formed adjacent to causative intrusive complexes, and the stock-hosted Llallagua xenothermal deposit (Fig. 1B)
663 relative to epithermal and shallow xenothermal deposits formed at lower temperatures and depths (Figs. 1, 3).

664 A decrease in Ti and Ti/Zr in cassiterite grains has been linked to transition from proximal (higher temperature) to
665 distal (lower temperature) locations in intrusion-centered hydrothermal systems (Taylor 1979; Cheng et al. 2019),
666 which coincides with a higher solubility of Zr in hydrothermal fluids compared to Ti (see also Kessel et al. 2005).
667 On the other hand, Sc is said to be transported as F complexes in post-magmatic fluids (Plimer et al. 1991). Our
668 samples describe Ti/Zr variations by up to two orders of magnitude and systematically plot above the 1:1 ratio line
669 in Fig. 4E similar to reference data for xenothermal and epithermal deposits. In general, cassiterite samples from
670 the intrusion-proximal Kellhuani and Viloco deposits show higher Ti/Zr and Ti/Sc than samples from the
671 intrusion-distal Ánimas - Chocaya - Siete Suyos and Poopó deposits (Figs. 1B, 4E,G). Accordingly, our dataset
672 agrees with a progressive depletion of Ti relative to Zr and Sc in hydrothermal fluids as they evolved or migrated
673 away from the causative intrusive bodies and hence the Ti/Zr and Ti/Sc ratios can be used as tracers to magmatic-
674 hydrothermal centers.

675 Cassiterite samples from the Bolivian tin belt yield a fair positive correlation between V and Sc, which has been
676 used to propose a $Sc^{3+}+V^{5+} \Leftrightarrow 2Sn^{4+}$ coupled substitution in tin-granite-, greisen-, skarn- and vein-type ores by
677 Cheng et al. (2019). The behavior in hydrothermal systems of elements such as V, In, Ge and Ga regarding
678 cassiterite is poorly understood. Plimer et al. (1991) related the In composition of cassiterite directly to the
679 concentration of this element in the hydrothermal ore-forming fluids. The highest average concentrations of In in
680 cassiterite samples from the Bolivian tin belt are found indeed in Huari Huari and Ánimas - Chocaya - Siete Suyos
681 districts, which are well known for their high concentrations of In (Schwarz-Schampera and Herzig 2002; Torró et
682 al. 2019a,b; Pring et al. 2020; Tables 2 and 3) thus supporting this idea. Lerouge et al. (2019) found that sulfides
683 (such as stannite and sphalerite) and rutile associated with In-poor cassiterite contain high amounts of In thus
684 highlighting that In tends to preferentially partition in sulfides rather than cassiterite. This would be also the case
685 in the deposits from the Bolivian tin belt (Jiménez-Franco et al. 2018; Cacho et al. 2019; Torres et al. 2019; Torró
686 et al. 2019a,b).

687 The studied cassiterite samples from the Bolivian tin belt show average REE concentrations similar to those of
688 reference data for cassiterite in granite, granite-cupola and greisen mineralizations (Table 1; Fig. 5). Similar to
689 cassiterite from the Bolivian tin belt, cassiterite from granites and granite-cupolas also show positive anomalies in
690 MREE in chondrite-normalized diagrams, particularly Tb (see Zoheir et al. 2019). It is noteworthy that, unlike
691 cassiterite from the Bolivian tin belt, cassiterite compositions reported in the literature normally lack negative Ce
692 anomalies. Broken, "unusual" REE patterns combining concave and convex tetrads are acknowledged in tin-
693 bearing magmatic-hydrothermal systems probably connected to liquid-vapor REE fractionation (Monecke et al.
694 2011). Following Monecke et al. (2011), the irregular REE tetrad partition in cassiterite samples from the Bolivian
695 tin belt would reflect generalized fluid immiscibility during the early stages of evolution of the studied deposits
696 concomitant with the crystallization of cassiterite. Kelly and Turneaure (1970) proposed that boiling of the early
697 tin-bearing fluid was an important mechanism for the precipitation of early quartz and cassiterite in Llallagua, and
698 may have played an important role in the location of high grade ore in some shallow deposits of central and
699 southern Bolivia (as also suggested by Chace 1948a,b for the Oruro deposits). These authors suggest that the
700 upward vertical zoning of high grade cassiterite to low grade sulfide-rich tin ore may mark levels of local boiling.
701 Other plausible mechanisms that might have controlled REE fractionation during the crystallization of
702 hydrothermal cassiterite in Bolivian deposits include i) mixing between magmatic and meteoric waters (as
703 proposed for the San Rafael deposit; Kontak and Clark 2002, Harlaux et al. 2020) leading to destabilization of
704 REE chloride and fluoride complexes, which are more stable with increasing atomic number (Migdisov et al.
705 2016); and ii) partitioning of REE between co-crystallizing phases (e.g., monazite and tourmaline; Jolliff et al.
706 1987; Harlaux et al. 2020; Sciuba et al. 2020). Nevertheless, these alternative or complimentary mechanisms
707 leading to REE fractionation would not reproduce the broken, highly irregular chondrite-normalized REE patterns
708 described here for cassiterite samples from the Bolivian tin belt and therefore we surmise that their impact, if any,
709 was subordinate to that of fluid immiscibility.

710 **Potential of cassiterite from the Bolivian tin belt as a source of critical elements as byproducts**

711 Previous studies on the concentration of high-tech metals in deposits from the Bolivian tin belt have focused
712 mostly on the sulfide mineralization (Schwarz-Schampera and Herzig 2002; Ishihara et al. 2011; Artiaga et al.
713 2013; Murakami and Ishihara 2013; Jiménez-Franco et al. 2018; Cacho et al. 2019; Torres et al. 2019; Torró et al.
714 2019a,b; Pring et al. 2020; summary of reported maximum concentrations of In, Ge and Ga shown in Table 3). In

715 the following lines we assess the potential of cassiterite from the Bolivian tin belt as a source of high-tech, critical
716 elements, chiefly Nb, Ta, In, Ge and Ga, by comparing our results with bibliographic values.

717 Cassiterite samples from the Bolivian tin belt yielded much lower Nb concentrations than cassiterite from granite-
718 hosted, granite cupola, greisen and pegmatite mineralizations worldwide (Table 2). Cassiterite from xenothermal
719 and epithermal mineralizations reported in the literature is also enriched in Nb relative to our values. Likewise,
720 cassiterite from the Bolivian tin belt is strongly depleted in Ta relative to most cassiterite compositions reported in
721 the literature (Table 2). According to our results, cassiterite from the Bolivian tin belt is not likely to make a good
722 resource for these two metals.

723 Indium concentrations in cassiterite from the Bolivian tin belt are consistent with, and often higher than,
724 previously reported concentrations worldwide. However, it is noteworthy that in most of the studied Bolivian
725 deposits, sulfide minerals, namely sphalerite and stannite, are the main In hosts, often with concentrations at the
726 wt% level (Table 3). On the other hand, there is a close correlation between In enrichment in cassiterite and sulfide
727 minerals in deposits along the Bolivian tin belt (Table 3). Therefore, in some deposits, cassiterite might represent a
728 potential, additional source of In. The metallurgical recovery of In from cassiterite is, as far as we know, poorly
729 developed. Preconcentration of In in slag during the smelting process to obtain tin metal from cassiterite could be
730 expected, just as for Nb and Ta (Gupta and Suri 1994), In being separated afterwards by a multistep operation
731 involving sulfuric acid leach of ferrite slag (Tshijik Karumb 2016).

732 Gallium contents in cassiterite samples from the Bolivian tin belt are also consistent with and often higher than
733 concentrations reported in the literature (Table 2). Germanium concentrations in the studied samples of cassiterite
734 are systematically very low, particularly if compared to Ge concentrations reported for cassiterite from pegmatites.
735 With data in hand, cassiterite from the Bolivian tin belt is probably unattractive as source of Ge.

736 **Conclusions**

737 Tin mineralization has been dated directly by U-Pb geochronology on cassiterite samples from the Kellhuani
738 (218.3 ± 5.5 Ma), Viloco (24.4 ± 0.4 Ma), Huanuni (24.0 ± 2.4 Ma) and Llallagua (24.0 ± 5.1 Ma) deposits. The
739 dates are in good agreement with published ages for igneous rocks within the respective districts and confirm that
740 hydrothermal tin mineralization in the Bolivian tin belt occurred mostly in two periods: Late Triassic and Late
741 Oligocene –Miocene.

742 Our new ages closely coincide with two major magmatic episodes that were apparently triggered by mantle
743 upwelling, decompression melting and basalt production, and related high heat flow into the overlying crust. The
744 age obtained for Kellhuani coincides with the culmination of the Mitu rifting episode (~240–220 Ma; Spikings et
745 al. 2016). The dates obtained for Viloco, Huanuni and Llallagua have mean values at 24.0 Ma, which overlap with
746 the timing of major and widespread basaltic magmatism in the central Altiplano and probably adjacent regions.

747 The convergence of highly evolved, peraluminous silicic melts derived in part from the melting of volatile-rich
748 sedimentary series and a sustained heat and fluid contribution from primitive melts stored at intermediate and
749 upper levels of a thickened continental crust enhanced the formation of large tin deposits along the Bolivian tin
750 belt.

751 The composition of the studied cassiterite samples is relatively homogeneous at the metalliferous belt scale.
752 Nevertheless, nuances in trace element contents in mineralizations emplaced at different levels within the
753 xenothermal and epithermal environments allow for the identification of some compositional trends. Some
754 deposits formed adjacent to causative intrusive complexes such as Kellhuani, Viloco and Llallagua are typically
755 enriched in Nb and Ta relative to epithermal and shallow xenothermal deposits. In addition, Ti/Zr and Ti/Sc ratios
756 decrease from intrusive-proximal to intrusive-distal locations and therefore can be used to vectorize toward
757 magmatic-hydrothermal centers.

758 REE abundances are elevated in cassiterite from intrusive-proximal (e.g., Kellhuani, Llallagua) relative to
759 intrusive-distal mineralizations. There is a general, pronounced enrichment in MREE relative to LREE and HREE
760 in chondrite-normalized patterns. REE distribution patterns are likely influenced by boiling processes, which yield
761 characteristic broken REE patterns combining concave and convex tetrads.

762 The hydrothermal cassiterite from the Bolivian tin belt has low Nb and Ta compared with magmatic cassiterite in
763 rare-metal granites and pegmatites. The concentration of Ge is systematically very low in the studied cassiterite
764 samples. However, some cassiterite samples have relatively high concentrations of In and Ga. Interestingly, the
765 highest In concentrations in cassiterite from the Bolivian tin belt are found in samples from deposits with
766 documented high concentration of this element in sulfide minerals, suggesting that the concentration of In in
767 cassiterite is primarily controlled by its availability in the hydrothermal fluid. In these particular deposits,
768 cassiterite could represent an additional economic source of In.

Acknowledgments

This study was economically supported by the Peruvian CONCYTEC-FONDECYT-World Bank project 107-2018-FONDECYT-BM-IADT-AV and the Catalan project 2017-SGR-00707. We gratefully acknowledge Pura Alfonso (Polytechnic University of Catalonia) for providing cassiterite samples from the Llallagua deposit. The Bolivian State Mining Company (Corporación Minera de Bolivia—COMIBOL) granted its permission to the authors to access the Huanuni mine and to perform the necessary sampling; J.C. Ayaviri, J. Araca, R. Condori, N. Guevara and all individuals at COMIBOL are cordially thanked for their kind and efficient help during field work. The help and hospitality extended by the miners from mining cooperatives during sampling and field work are most gratefully acknowledged. We appreciate the technical support by Xavier Llovet (CCiT-UB) during the acquisition of EPMA data, and by Peter Tollan (ETH) during the acquisition of LA-ICP-MS data. We are grateful to Daniel Kontak, Matthieu Harlaux, and Editor-in-Chief Bernd Lehmann for their constructive comments which significantly improved the manuscript.

References

Abdalla HM, Matsueda H, Obeid MA, Takahashi R (2008) Chemistry of cassiterite in rare metal granitoids and the associated rocks in the Eastern Desert, Egypt. J Miner Petrol Sci 103:318-326. https://doi.org/10.2465/jmps.070528a

Ahlfeld F (1967) Metallogenetic epochs and provinces of Bolivia. Miner Deposita 2:291–311. https://doi.org/10.1007/BF00207022

Ahlfeld F, Branisa L (1960) Geología de Bolivia. Don Bosco, Texas

Ahlfeld F, Schneider-Scherbina A (1964) Los yacimientos minerales y de hidrocarburos de Bolivia. Bolivia Departamento Nacional de Geología 5:1–388

Arce-Burgoa O (2009) Metalliferous Ore Deposits of Bolivia. SPC Impresores: La Paz

Arce-Burgoa O, Goldfarb RJ (2009) Metallogeny of Bolivia. SEG Newsletter 79:1–15

Artiaga D, Torres B, Torró L, Tauler E, Melgarejo JC, Arce-Burgoa O (2013) The Viloco Sn-W-Mo-As deposits, Bolivia: geology and mineralogy. Conference: 12th SGA Biennial Meeting "Mineral deposit research for a high-tech world", 3:1239–1242, Uppsala

Baldellón E, Fornari M, Espinoza F, Soler P (1994) Sucesión estructural de la zona Serranía de las Minas. XI Congreso Geológico de Bolivia, Memorias, pp. 238–247

Bau M (1996) Controls on the fractionation of isovalent trace elements in magmatic and aqueous systems: evidence from Y/Ho, Zr/Hf, and lanthanide tetrad effect. Contrib Mineral Petrol 123:323-333. https://doi.org/10.1007/s004100050159

Betkowski WB, Rakovan J, Harlov DE (2017) Geochemical and textural characterization of phosphate accessory phases in the vein assemblage and metasomatically altered Llallagua tin porphyry. Miner Petrol 111:547–568. https://doi.org/10.1007/s00710-017-0510-6

Briskey JA (2005) Indium in lead–zinc and other mineral deposits. Open File Rpt 2005-1209. http://pubs.usgs.gov/of/2005/1209/2005-1209.pdf. Accessed 10 June 2020

Buddington AF (1935) High-temperature mineral associations at shallow to moderate depths. Econ Geol 30:205–222. https://doi.org/10.2113/gsecongeo.30.3.205

Cacho A, Melgarejo JC, Camprubí A, Torró L, Castillo-Oliver M, Torres B, Artiaga D, Tauler E, Martínez Á, Campeny M, Alfonso P, Arce-Burgoa OR (2019) Mineralogy and distribution of critical elements in the Sn–W–Pb–Ag–Zn Huanuni deposit, Bolivia. Minerals 9:753. https://doi.org/10.3390/min9120753

Chace FM (1948a) Tin-silver veins of Oruro, Bolivia, Part I. Econ Geol 43:333–383. https://doi.org/10.2113/gsecongeo.43.5.333

Chace FM (1948b) Tin-silver veins of Oruro Bolivia; Part II. Econ Geol 43:435–470. https://doi.org/10.2113/gsecongeo.43.6.435

Cheilletz A, Clark AH, Farrar E, Arroyo Pauca G, MacArthur JD, Pichavant M (1990) Stratigraphy and geochronology of the Macusani ignimbrite field: chronometer of the Mio-Pliocene geodynamic evolution of the Andes of SE Peru. In: Symposium international "Géodynamique andine": résumés des communications. Paris: ORSTOM, 341–344

Chen LL, Ni P, Dai BZ, Li WS, Chi Z, Pan JY (2019) The genetic association between quartz vein- and greisen-type mineralization at the Maoping W–Sn deposit, Southern Jiangxi, China: Insights from zircon and cassiterite U–Pb Ages and cassiterite trace element composition. Minerals 9:411. https://doi.org/10.3390/min9070411

Cheng Y, Spandler C, Kemp A, Mao J, Rusk B, Hu Y, Blake K (2019) Controls on cassiterite (SnO_2) crystallization: Evidence from cathodoluminescence, trace-element chemistry, and geochronology at the Gejiu Tin District. Am Mineral 104:118–129. https://doi.org/10.2138/am-2019-6466

Clark AH, Farrar E (1973) The Bolivian Tin Province; notes on the available geochronological data. Econ Geol 68:102–106. https://doi.org/10.2113/gsecongeo.68.1.102

Clark AH, Farrar E, Caelles JC, Haynes SJ, Lortie RB, McBride SL, Quirt GS, Robertson RCR, Zentilli M (1976) Longitudinal variations in the metallogenetic evolution of the central Andes: A progress report. Geol S Am S 14:23–58

Clark AH, Palma VV, Archibald DA, Farrar E, Robertson RCR (1983) Occurrence and age of tin mineralization in the Cordillera Oriental, southern Peru. Econ Geol 78:514-520. https://doi.org/10.2113/gsecongeo.78.3.514

Clark AH, Farrar E, Kontak DJ, Langridge RJ, Arenas FMJ, France LJ, McBride SL, Woodman PL, Wasteneys HA, Sandeman HA, Archibald DA (1990) Geologic and geochronologic constraints on the metallogenic evolution of the Andes of southeastern Peru. Econ Geol 85:1520–1583. https://doi.org/10.2113/gsecongeo.85.7.1520

836 Clark AH, Chen Y, Grant JW, Kontak DJ, Wasteneys HA, Sandeman HA, Farrar E, Archibald DE (2000) Delayed
837 inception of ore deposition in major lithophile-metal vein systems: The San Rafael tin and Pasto Bueno
838 tungsten deposits, Peru. Geol S Am S 32, pp. 279

839 Claure H, Olivera L, Heuschmidt B, Arduz M, Troëng B, Ballón R (1996) Mapas temáticos de recursos minerales
840 de Bolivia, Hoja Uncía: Bol Ser Geol Bolivia 7:184

841 Cordani UG, Iriarte AR, Sato K (2019) Geochronological systematics of the Huayna Potosí, Zongo and Taquesi
842 plutons, Cordillera Real of Bolivia, by the K/Ar, Rb/Sr and U/Pb methods. Braz J Geol 49:1-22.
843 https://doi.org/10.1590/2317-4889201920190016

844 Cunningham CG, Zartman RE, McKee EH, Rye RO, Naeser CW, Sanjinés V, Ericksen GE, Tavera V (1996) The
845 age and thermal history of Cerro Rico de Potosi, Bolivia. Miner Deposita 31:374-385.
846 https://doi.org/10.1007/BF00189185

847 DeCelles PG, Horton BK (2003) Early to middle Tertiary foreland basin development and the history of Andean
848 crustal shortening in Bolivia. Geol Soc Am Bull 115:58-77. https://doi.org/10.1130/0016-
849 7606(2003)115%3C0058:ETMTFB%3E2.0.CO;2

850 Demouy S, Paquette J-L, Saint-Blanquat M de, Benoit M, Belousova EA, O'Reilly SY, García F, Tejada LC,
851 Gallegos R, Sempere T (2012) Spatial and temporal evolution of Liassic to Paleocene arc activity in
852 southern Peru unraveled by zircon U-Pb and Hf in-situ data on plutonic rocks. Lithos 155:183–200.
853 https://doi.org/10.1016/j.lithos.2012.09.001

854 de Silva SL, Kay MS (2018) Turning up the heat: High-flux magmatism in the Central Andes. Elements 14:245–
855 250. https://doi.org/10.2138/gselements.14.4.245

856 Díaz E (1997) Facies y ambientes sedimentarios de la Formación Cancañiri (Silúrico inferior) en La Cumbre de La
857 Paz, norte de la Cordillera Oriental de Bolivia. Geogaceta 22:55-57

858 Dietrich A, Lehmann B, Wallianos A (2000) Bulk rock and melt inclusion geochemistry of Bolivian tin porphyry
859 systems. Econ Geol 95:313-326. https://doi.org/10.2113/gsecongeo.95.2.313

860 European Commission (2017) Critical Raw Materials. https://ec.europa.eu/growth/sectors/raw-materials/specific-
861 interest/critical_en. Accessed 14 April 2020

862 Everden JF (1961) Edades absolutas de algunas rocas ígneas en Bolivia por el método potasio-argón. Soc Geol Bol
863 Not 2:3

864 Evernden JF, Kriz SJ, Cherroni CM (1977) Potassium-argon ages of some Bolivian rocks. Econ Geol 72:1042–
865 1061. https://doi.org/10.2113/gsecongeo.72.6.1042

866 Farrar E, Clark AH, Kontak DJ, Archibald DA (1988) Zongo-San Gabán zone: Eocene foreland boundary of the
867 Central Andean orogen, northwest Bolivia and southeast Peru. Geology 16:55–58.
868 https://doi.org/10.1130/0091-7613(1988)016%3C0055:ZSGNZE%3E2.3.CO;2

869 Farrar E, Clark AH, Heinrich SM (1990) The age of the Zongo pluton and the tectonothermal evolution of the
870 Zongo-San Gabán Zone in the Cordillera Real, Bolivia. Extended abstracts, 1st International Symposium
871 on Andean Geodynamics, Grenoble, pp. 171–174

872 Fontboté L (2018) Ore deposits of the Central Andes. Elements 14:257–261.
873 https://doi.org/10.2138/gselements.14.4.257

874 Fornari M, Baldellón E, Espinoza F, Ibarra I, Jiménez N, Mamani M (2002) Ar-Ar dating of Late Oligocene-Early
875 Miocene volcanism in the Altiplano. Extended abstracts, 4th International Symposium on Andean
876 Geodynamics, Toulouse, pp. 223–226

877 Fuchsloch W, Nex P, Kinnaird J (2019) The geochemical evolution of Nb-Ta-Sn oxides from pegmatites of the
878 Cape Cross–Uis pegmatite belt, Namibia. Mineral Mag 83:1-56. https://doi.org/10.1180/mgm.2018.151

879 Gillis RJ, Horton BK, Grove M (2006) Thermochronology, geochronology, and upper crustal structure of the
880 Cordillera Real: implications for Cenozoic exhumation of the central Andean plateau. Tectonics 25:1–22.
881 https://doi.org/10.1029/2005TC001887

882 Goldschmidt V (1913) Atlas der Kristallformen. Heidelberg

883 Gordon SG (1944) The mineralogy of the tin mines of Cerro de Llallagua, Bolivia. Proc Acad Nat Sci Philadelphia
884 96:279–359

885 Gorelikova NV, Khanchuk AI, Bortnikov NS, Pawlowsky-Glahn V, Tolosana-Delgado R (2004) Classification of
886 tin deposits using trace elements in cassiterites (Far East, Russia) In Proceedings of the Interim Iagod
887 Conference Vladivostok, Russia. Dal'nauka, 590–593

888 Gorelikova NV, Tolosana-Delgado R, Pawlowsky-Glahn V, Khanchuk A, Gonevchuk V (2006) Discriminating
889 geodynamical regimes of tin ore formation using trace element composition of cassiterite: The Sikhote'Alin
890 case (Far Eastern Russia). Geol Soc Lon Spec Publ 264:43–57.
891 https://doi.org/10.1144/GSL.SP.2006.264.01.04

892 Grant JN, Halls C, Salinas WA, Snelling NJ (1979) K-Ar ages of igneous rocks and mineralization in part of the
893 Bolivian tin belt. Econ Geol 74:838–851. https://doi.org/10.2113/gsecongeo.74.4.838

894 Guillong M, Hametner K, Reusser E, Wilson SA, Günther D (2005) Preliminary characterisation of new glass
895 reference materials (GSA- 1G, GSC- 1G, GSD- 1G and GSE- 1G) by Laser Ablation- Inductively
896 Coupled Plasma- Mass Spectrometry using 193 nm, 213 nm and 266 nm wavelengths. Geostand Geoanal
897 Res 29:315-331. https://doi.org/10.1111/j.1751-908x.2005.tb00903.x

898 Guillong M, Meier DL, Allan MM, Heinrich CA, Yardley BWD (2008) SILLS: A MATLAB-based program for
899 the reduction of laser ablation ICP-MS data of homogeneous materials and inclusions. In: Sylvester P, (ed)
900 Laser Ablation ICP-MS in the Earth Sciences: Current Practices and Outstanding Issues. Miner Assoc Can.
901 Short Course 40

902 Guillong M, Wotzlaw JF, Looser N, Laurent O (2020) Evaluating the reliability of U–Pb laser ablation inductively
903 coupled plasma mass spectrometry (LA-ICP-MS) carbonate geochronology: matrix issues and a potential
904 calcite validation reference material. Geochronology 2:155-167. https://doi.org/10.5194/gchron-2-155-2020

905 Guo J, Zhang RQ, Sun WD, Ling MX, Hu YB, Wu K, Zhang LC (2018) Genesis of tin-dominant polymetallic
906 deposits in the Dachang district, South China: insights from cassiterite U-Pb ages and trace element
907 compositions. Ore Geol Rev 95:863–879. https://doi.org/10.1016/j.oregeorev.2018.03.023

908 Gupta CK, Suri AK (1994) Extractive metallurgy of niobium. CRC press inc., Florida

909 Harlaux M, Kouzmanov K, Gialli S, Laurent O, Rielli A, Dini A, Chauvet A, Menzies A, Kalinaj M, Fontboté L
910 (2020) Tourmaline as a Tracer of Late-Magmatic to Hydrothermal Fluid Evolution: The World-Class San
911 Rafael Tin (-Copper) Deposit, Peru. Econ Geol, in press. https://doi.org/10.5382/econgeo.4762

912 Hellstrom JC, Paton C, Woodhead JD, Hergt JM (2008) Iolite: Software for spatially resolved LA-(quad and MC)
913 ICP-MS analysis. In: Sylvester P (ed) Laser ablation ICP-MS in the Earth sciences: Current practices and
914 outstanding issues. Miner Assoc Can 40:343–348

915 Heuschmidt B, La Torre JB, Angels VM, Zapata MC (2002) Las áreas prospectivas de Bolivia para yacimientos
916 metalíferos. Boletín del Servicio Nacional de Geología y Minería, 30, La Paz

917 Horton BK, Hampton BA, Waanders GL (2001) Paleogene synorogenic sedimentation in the Altiplano plateau and
918 implications for initial mountain building in the central Andes. Geol Soc Am Bull 113:1387–1400.
919 https://doi.org/10.1130/0016-7606(2001)113%3C1387:PSSITA%3E2.0.CO;2

920 Hoskin PWO, Schaltegger U (2003) The composition of zircon and igneous and metamorphic petrogenesis. Rev
921 Mineral Geochem 53: 27–62. https://doi.org/10.2113/0530027

922 Hulsbosch N, Muchez P (2019) Tracing fluid saturation during pegmatite differentiation by studying the fluid
923 inclusion evolution and multiphase cassiterite mineralisation of the Gatumba pegmatite dyke system (NW
924 Rwanda). Lithos 354-355, Article 105285. https://doi.org/10.1016/j.lithos.2019.105285

925 Husson L, Sempere T (2003) Thickening the Altiplano crust by gravity-driven crustal channel flow. Geophys Res
926 Lett 30:1243-1246. https://doi.org/10.1029/2002GL016877

927 Imai H, Lee MS, Iida K, Fujiki Y, Takenouchi S (1975) Geologic structure and mineralization of xenothermal
928 vein-type deposits in Japan. Econ Geol 70:647–676. https://doi.org/10.2113/gsecongeo.70.4.647

929 Isacks BL (1988) Uplift of the central Andean plateau and bending of the Bolivian orocline. J Geophys Res
930 93:3211–3231. https://doi.org/10.1029/JB093iB04p03211

931 Ishihara S (1981) The granitoid series and mineralization. Econ Geol Anniversary Vol 75:458-484.
932 https://doi.org/10.5382/AV75.14

933 Ishihara S, Murakami H, Márquez-Zavalia MF (2011) Inferred indium resources of the Bolivian tin-polymetallic
934 deposits. Resour Geol 61:174-191. https://doi.org/10.1111/j.1751-3928.2011.00157.x

935 James DE (1971a) Andean crustal and upper mantle structure. J Geophys Res 76:3246–3271.
936 https://doi.org/10.1029/JB076i014p03246

937 James DE (1971b) Plate tectonic model for the evolution of the Central Andes. Geol Soc Am Bull 82:3325–3346.
938 https://doi.org/10.1130/0016-7606(1971)82[3325:PTMFTE]2.0.CO;2

939 Jiang SY, Yu JM, Lu JJ (2004) Trace and rare-earth element geochemistry in tourmaline and cassiterite from the
940 Yunlong tin deposit, Yunnan, China: Implication for migmatitic-hydrothermal fluid evolution and ore
941 genesis. Chem Geol 209:193–213. https://doi.org/10.1016/j.chemgeo.2004.04.021

Jiménez-Franco A, Alfonso P, Canet C, Trujillo JE (2018) Mineral chemistry of In-bearing minerals in the Santa Fe mining district, Bolivia. Andean Geol 45:410–432. https://doi.org/10.5027/andgeoV45n3-3052

Jochum KP, Wies U, Stoll B, Kuzmin D, Yang Q, Raczek I, Jacob DE, Stracke A, Birbaum K, Frick DA, Günter D, Enzweiler J (2011) Determination of reference values for NIST SRM 610-617 glasses following ISO guidelines. Geostand Geoanal Res 35:397–429. https://doi.org/10.1111/j.1751-908X.2011.00120.x

Jolliff BL, Papike JJ, Laul JC (1987) Mineral recorders of pegmatite internal evolution: REE contents of tourmaline from the Bob Ingersoll pegmatite, South Dakota. Geochim Cosmochim Ac 51:2225-2232. https://doi.org/10.1016/0016-7037(87)90272-9

Kelly WC, Turneaure FS (1970) Mineralogy, paragenesis and geothermometry of the tin and tungsten deposits of the Eastern Andes, Bolivia. Econ Geol 65:609–680. https://doi.org/10.2113/gsecongeo.65.6.609

Kendall-Langley L, Kemp A, Grigson J, Hammerli J (2019) U-Pb and reconnaissance Lu-Hf isotope analysis of cassiterite and columbite group minerals from Archean Li-Cs-Ta type pegmatites of Western Australia. Lithos 352-353. Article 105231. https://doi.org/10.1016/j.lithos.2019.105231

Kessel R, Ulmer P, Pettke T, Schmidt MW, Thompson AB (2005) The water-basalt system at 4 to 6 GPa: Phase relations and second critical endpoint in a K-free eclogite at 700 to 1400 °C. Earth Planet Sci Lett 237:873–892. https://doi.org/10.1016/j.epsl.2005.06.018

Keutsch F, De Brodtkorb MK (2008) Metalliferous paragenesis of the San José mine, Oruro, Bolivia. J S Am Earth Sci 25:485-491. https://doi.org/10.1016/j.jsames.2007.12.003

Koeppen RP, Smith RL, Kunk MJ, Flores AM, Luedke RG, Sutter JF (1987) The Morococala volcanics: Highly peraluminous rhyolite ash flow magmatism in the Cordillera Oriental, Bolivia. Geol S Am S 19:731

Kohn MJ, Vervoort JD (2008) U-Th-Pb dating of monazite by single collector ICP-MS: pitfalls and potential. Geochem Geophys Geosyst 9:1–16. https://doi.org/10.1029/2007GC001899

Kono M, Fukao Y, Yamamoto A (1989) Mountain building in the Central Andes. J Geophys Res 94:3891–3905. https://doi.org/10.1029/JB094iB04p03891

Kontak DJ, Clark AH (2002) Genesis of the giant, bonanza San Rafael lode tin deposit, Peru: Origin and significance of pervasive alteration. Econ Geol 97:1741–1777. https://doi.org/10.2113/gsecongeo.97.8.1741

Kontak DJ, Clark AH, Farrar E, Strong DF (1984) The rift-associated Permo-Triassic magmatism of the Eastern Cordillera: A precursor to the Andean orogeny. In Pitcher WS, Atherton MP, Cobbing EJ, Beckinsale RD (eds) Magmatism at a plate edge: The Peruvian Andes. Blackie, Glasgow-London

Kontak DJ, Clark AH, Pearce TH, Strong DF, Baadsgaard H (1986) Petrogenesis of a Neogene shoshonite suite, Cerro Moromoroni, Puno, southeastern Peru. Can Mineral 24:117-135

Kontak DJ, Clark AH, Farrar E, Archibald DA, Baadsgaard H (1987) Geochronological data for Tertiary granites of the southeast Peru segment of the central Andean tin belt. Econ Geol 82:1711-1618. https://doi.org/10.2113/gsecongeo.82.6.1611

976 Kontak DJ, Farrar E, Clark AH, Archibald DA (1990) Eocene tectono-thermal rejuvenation of an upper Paleozoic-
977 lower Mesozoic terrane in the Cordillera de Carabaya, Puno, southeastern Peru, revealed by K-Ar and
978 $^{40}Ar/^{39}Ar$ dating. J S Am Earth Sci 3:231–246. https://doi.org/10.1016/0895-9811(90)90005-L

979 Lamb S, Hoke L (1997) Origin of the high plateau in the Central Andes, Bolivia, South America. Tectonics
980 16:623–649. https://doi.org/10.1029/97TC00495

981 Lancelot JR, Laubacher G, Marocco R, Renaud U (1978) U/Pb radiochronology of two granitic plutons from the
982 Eastern Cordillera (Peru): Extent of Permian magmatic activity and consequence Geol Rundsch 67:286-
983 248. https://doi.org/10.1007/BF01803263

984 Legros H, Harlaux M, Mercadier J, Romer RL, Poujol M, Camacho A, Marignac C, Cuney M, Wang RC, Charles
985 N, Lespinasse MY (2020) The world-class Nanling metallogenic belt (Jiangxi, China): W and Sn
986 deposition at 160 Ma followed by 30 m.y. of hydrothermal metal redistribution. Ore Geol Rev 117. Article
987 103302. https://doi.org/10.1016/j.oregeorev.2019.103302

988 Lehmann B (1985) Formation of the strata-bound Kellhuani tin deposits, Bolivia. Miner Deposita 20:169–176.
989 https://doi.org/10.1007/BF00204561

990 Lehmann B, Ishihara S, Michel H, Miller J, Rapela C, Sanchez A, Tistl M, Winkelmann L (1990) The Bolivian tin
991 province and regional tin distribution in the Central Andes: A reassessment. Econ Geol 85:1044–1058.
992 https://doi.org/10.2113/gsecongeo.85.5.1044

993 Lehmann B, Dietrich A, Heinhorst J, Métrich N, Mosbah M, Palacios C, Schneider HJ, Wallianos A, Webster J,
994 Winkelmann L (2000) Boron in the Bolivian tin belt. Miner Deposita 35:223-232.
995 https://doi.org/10.1007/s001260050017

996 Lehmann B, Zoheir B, Neymark L, Zeh A, Emam A, Radwan A, Zhang R, Moscati R (2020) Monazite and
997 cassiterite U-Pb dating of the Abu Dabbab rare-metal granite, Egypt: Late Cryogenian metalliferous granite
998 magmatism in the Arabian-Nubian Shield, Gondwana Res 84:71-80.
999 https://doi.org/10.1016/j.gr.2020.03.001

1000 Lentz D, McAllister A (1990) The petrogenesis of tin- and sulfide-lode mineralization at True Hill, southwestern
1001 New Brunswick. Atl Geol 26:136-155. https://doi.org/10.4138/1698

1002 Lerouge C, Gloaguen E, Wille G, Bailly L (2017) Distribution of In and other rare metals in cassiterite and
1003 associated minerals in Sn±W ore deposits of the western Variscan Belt. Eur J Mineral 29:739-753.
1004 https://doi.org/10.1127/ejm/2017/0029-2673

1005 Maffione M, Speranza F, Faccenna C (2009) Bending and growth of the Central Andean plateau: Paleomagnetic
1006 and structural constraints from the Eastern Cordillera (22-24°S, NW Argentina). Tectonics 28.
1007 https://doi.org/10.1029/2008TC002402

1008 Mao W, Zhong H, Yang J, Tang Y, Liu L, Fu Y, Zhang X, Sein K, Soe MA, Li J, Zhang Le (2020) Combined
1009 zircon, molybdenite, and cassiterite geochronology and cassiterite geochemistry of the Kuntabin tin-
1010 tungsten deposit in Myanmar. Econ Geol 115:603–625. https://doi.org/10.5382/econgeo.4713

1011 Martinez C, Vargas E (1990) Sobre las deformaciones sinsedimentarias mesozoicas de la región de Macha-
1012 Pocoata-Colquechaca (Norte de Potosí – Cordillera Oriental de Bolivia). YPFB 11:13-20

1013 McBride SL, Robertson RCR, Clark AH, Farrar E (1983) Magmatic and metallogenetic episodes in the northern
1014 tin belt, Cordillera Real, Bolivia. Geol Rundsch 72:685-71. https://doi.org/10.1007/BF01822089

1015 Migdisov A, Williams-Jones AE, Brugger J, Caporuscio FA (2016) Hydrothermal transport, deposition, and
1016 fractionation of the REE: Experimental data and thermodynamic calculations. Chem Geol 439:13-42.
1017 https://doi.org/10.1016/j.chemgeo.2016.06.005

1018 Mišković A, Spikings RA, Chew DM, Kosler J, Ulianov A, Schaltegger U (2009) Tectonomagmatic evolution of
1019 Western Amazonia: Geochemical characterization and zircon U-Pb geochronologic constraints from the
1020 Peruvian Eastern Cordilleran granitoids. Geol Soc Am Bull 121:1298–1324.
1021 https://doi.org/10.1130/B26488.1

1022 Mlynarczyk MSJ, Williams-Jones AE (2005) The role of collisional tectonics in the metallogeny of the Central
1023 Andean tin belt. Earth Planet Sc Lett 240:656- 667. https://doi.org/10.1016/j.epsl.2005.09.047

1024 Möller P, Dulski P, Szacki W, Malow G, Riedel E (1988) Substitution of tin in cassiterite by tantalum, niobium,
1025 tungsten, iron and manganese. Geochim Cosmochim Ac 52:1497-1503. https://doi.org/10.1016/0016-
1026 7037(88)90220-7

1027 Monecke T, Kempe U, Trinkler M, Thomas R, Dulski P, Wagner T (2011) Unusual rare earth element
1028 fractionation in a tin-bearing magmatic-hydrothermal system. Geology 39:295–298.
1029 https://doi.org/10.1130/G31659.1

1030 Moore F, Howie RA (1979) Geochemistry of some Cornubian cassiterites. Miner Deposita 14:103-7.
1031 https://doi.org/10.1007/BF00201869

1032 Morgan GB, London D, Luedke RG (1998) Petrochemistry of Late Miocene peraluminous silicic volcanic rocks
1033 from the Morococala Field, Bolivia. J Petrol 39:601-632 https://doi.org/10.1093/petroj/39.4.601

1034 Moscati R, Neymark L (2019) U–Pb geochronology of tin deposits associated with the Cornubian Batholith of
1035 southwest England: Direct dating of cassiterite by in situ LA-ICPMS. Miner Deposita 55:1-20.
1036 https://doi.org/10.1007/s00126-019-00870-y

1037 Müller B, Frischknecht R, Seward T, Heinrich C, Camargo Gallegos W (2001) A fluid inclusion reconnaissance
1038 study of the Huanuni tin deposit (Bolivia), using LA-ICP-MS micro-analysis. Miner Deposita 36:680–688.
1039 https://doi.org/10.1007/s001260100195

1040 Murakami H, Ishihara S (2013) Trace elements of Indium-bearing sphalerite from tin- polymetallic deposits in
1041 Bolivia, China and Japan: A femto-second LA-ICPMS study. Ore Geol Rev 53:223-243.
1042 https://doi.org/10.1016/j.oregeorev.2013.01.010

1043 Murciego A, Sanchez AG, Dusausoy Y, Pozas JM, Ruck R (1997) Geochemistry and EPR of cassiterites from the
1044 Iberian Hercynian Massif. Mineral Mag 61:357-365. https://doi.org/10.1180/minmag.1997.061.406.03

Murray BP, Horton BK, Matos R, Heizler MT (2010) Oligocene-Miocene basin evolution in the northern Altiplano, Bolivia: Implications for evolution of the central Andean backthrust belt and high plateau. Geol Soc Am Bull 122:1443–1462. https://doi.org/10.1130/B30129.1

Nascimento T, Souza V (2017) Mineralogy, stable isotopes ($\delta^{18}O$ and $\delta^{34}S$) and ^{40}Ar-^{39}Ar geochronology studies on the hydrothermal carapace of the Igarapé Manteiga W-Sn deposit, Rondônia. Braz J Geol 47:591-613. https://doi.org/10.1590/2317-4889201720170068

Neiva A (2008) Geochemistry of cassiterite and wolframite from tin and tungsten quartz veins in Portugal. Ore Geol Rev 33:221–238. https://doi.org/10.1016/j.oregeorev.2006.05.013

Nespolo M, Souvignier B (2015) Structural rationale for the occurrence of the elbow twins in cassiterite and rutile. J Miner Petrol Sci 110:157-165. https://doi.org/10.2465/jmps.150123

Neymark L, Holm-Denoma C, Moscati R (2018) In situ LA-ICPMS U–Pb dating of cassiterite without a known-age matrix-matched reference material: Examples from worldwide tin deposits spanning the Proterozoic to the Tertiary. Chem Geol 483:410-425. https://doi.org/10.1016/j.chemgeo.2018.03.008

Nupen S (2019) Mineral resource estimates for the Falchani lithium project in the Puno district of Peru. Prepared for Plateau Energy Metals Inc. under the Guidelines of National Instrument 43-101 and accompanying documents NI 43-101.F1 and NI 43-101.CP. Report No: C-MYI-EXP-1727-1134

Pastor M, Pastor A, Torró L, Martínez A, Artiaga D, Torres B, Tauler E, Melgarejo JC, Paillo F, Arce-Burgoa OR, Alfonso P (2015). The San José-Itos mines, Oruro, Bolivia: Structure and Ag-Sn mineralization. Abstracts, 13th SGA Biennial Meeting, Nancy, 1:327–330

Paton C, Woodhead JD, Hellstrom JC, Hergt JM, Greig A, Maas R (2010) Improved laser ablation U-Pb zircon geochronology through robust downhole fractionation correction. Geochem Geophys Geosyst 11:1–36. https://doi.org/10.1029/2009GC002618

Pavlova GG, Palessky SV, Borisenko AS, Vladimirov AG, Seifert T, Phan L (2015) Indium in cassiterite and ores of tin deposits. Ore Geol Rev 66:99-113. https://doi.org/10.1016/j.oregeorev.2014.10.009

Petersen U (1970) Metallogenic Provinces in South America. Geol Rundsch 59:834–897. https://doi.org/10.1007/bf02042275

Petrus JA, Kamber BS (2012) VizualAge: A novel approach to Laser Ablation ICP-MS U-Pb geochronology data reduction. Geostand Geoanal Res 36:247–270. https://doi.org/10.1111/j.1751-908X.2012.00158.x

Picard D, Sempere T, Plantard O (2008) Direction and timing of uplift propagation in the Peruvian Andes deduced from molecular phylogenetics of highland biotaxa. Earth Planet Sc Lett 271:326-336. https://doi.org/10.1016/j.epsl.2008.04.024

Pichavant M, Herrera JV, Boulmier S, Briqueu L, Joron JL, Juteau M, Marin L, Michard A, Sheppard MFS, Treuil M, Vernet M (1987) The Macusani glasses, SE Peru: evidence of chemical fractionation in peraluminous magmas. In: Mysen BO (ed) Magmatic Processes: Physicochemical Principles. Geo Soc S P 1:359-374

1079 Pichavant M, Kontak DJ, Briqueu L, Herrera JV, Clark AH (1988a) The Miocene-Pliocene Macusani Volcanics,
1080 SE Peru I. Mineralogy and magmatic evolution of a two-mica aluminosilicate-bearing ignimbrite suite.
1081 Contrib Mineral Petr 100:300-324. https://doi.org/10.1007/BF00379742

1082 Pichavant M, Kontak DJ, Briqueu L, Herrera JV, Clark AH (1988b) The Miocene-Pliocene Macusani Volcanics,
1083 SE Peru II. Geochemistry and origin of a felsic peraluminous magma. Contrib Mineral Petr 100:325-338.
1084 https://doi.org/10.1007/BF00379742

1085 Plimer IR, Lu J, Kleeman JD (1991) Trace and rare earth elements in cassiterite - sources of components for the
1086 tin deposits of the Mole Granite, Australia. Miner Deposita 26:267–274
1087 https://doi.org/10.1007/BF00191072

1088 Pollard PJ, Pichavant M, Charoy B (1987) Contrasting evolution of fluorine- and boron-rich tin systems. Miner
1089 Deposita 22:315-321. https://doi.org/10.1007/BF00204525

1090 Poupeau G, Labrin E, Sabil N, Bigazzi G, Arroyo G, Vatin-Pérignon N (1993) Fission-track dating of 15
1091 macusanite glass pebbles from the Macusani volcanic field (SE Peru). Nucl Tracks Radiat Meas 21:499-
1092 506. https://doi.org/10.1016/1359-0189(93)90189-G

1093 Pring A, Wade B, McFadden A, Lenehan CE, Cook NJ (2020) Coupled substitutions of minor and trace elements
1094 in co-existing sphalerite and wurtzite. Minerals 10:147. https://doi.org/10.3390/min10020147

1095 Rakovan J, McDaniel DK, Reeder RJ (1997) Use of surface-controlled REE sectoral zoning in apatite from
1096 Llallagua, Bolivia, to determine a single-crystal SmNd age. Earth Planet Sci Lett 146:329–336.
1097 https://doi.org/10.1016/S0012-821X(96)00226-9

1098 Redwood S (1993) The Metallogeny of the Bolivian Andes. Mineral Deposit Research Unit Short Course No. 15
1099 University of British Columbia, Vancouver

1100 Redwood SD, MacIntyre RM (1989) K-Ar dating of Miocene magmatism and related epithermal mineralization of
1101 the northeastern Altiplano of Bolivia. Econ Geol 84:618–630. https://doi.org/10.2113/gsecongeo.84.3.618

1102 Reitsma MJ (2012) Reconstructing the Late Paleozoic–Early Mesozoic Plutonic and Sedimentary Record of
1103 South-East Peru: Orphaned Back-arcs Along the Western Margin of Gondwana. PhD thesis Terre &
1104 Environment 111. University of Geneva, Switzerland

1105 Revollo R (1967) Geología de la Cordillera de Santa Vera Cruz: Tesis de Grado, Universidad Mayor San Andrés,
1106 La Paz

1107 Rivas S, Carrasco R (1968) Geología y yacimientos minerales de la Region de Potosi. Bol Geol Bol 11

1108 Roperch P, Sempere T, Macedo O, Arriagada C, Fornari M, Tapia C, García M, Laj C (2006) Counterclockwise
1109 rotation of late Eocene–Oligocene fore- arc deposits in southern Peru and its significance for oroclinal
1110 bending in the central Andes. Tectonics 25:TC3010. https://doi.org/10.1029/2005TC001882

1111 Samson IM, Wood SA (2004) The rare earth elements: behaviour in hydrothermal fluids and concentration in
1112 hydrothermal mineral deposits, exclusive of alkaline settings. In: Linnen RL, Samson IM (eds) Rare
1113 element geochemistry and mineral deposits. Geological Association of Canada Short Course Notes. Geol
1114 Assoc Can 17:269-298

1115 Sandeman HA, Clark AH, Farrar E (1995) An integrated tectono-magmatic model for the evolution of the
1116 southern Peruvian Andes (13°-20°S) since 55 Ma. Int Geol Rev 37:1039–1073.
1117 https://doi.org/10.1080/00206819509465439

1118 Sandeman HA, Clark AH, Farrar E, Arroyo G (1997) Lithostratigraphy, petrology and $^{40}Ar/^{39}Ar$ geochronology of
1119 the Crucero Supergroup, Puno Department, SE Peru. J S Am Earth Sci 10:223–245.
1120 https://doi.org/10.1016/S0895-9811(97)00023-0

1121 Sciuba M, Beaudoin G, Makvandi S (2020) Chemical composition of tourmaline in orogenic gold deposits. Miner
1122 Deposita, In Press. https://doi.org/10.1007/s00126-020-00981-x

1123 Schildgen FT, Hoke DG (2018) The topographic evolution of the Central Andes. Elements 14:231–236.
1124 https://doi.org/10.2138/gselements.14.4.231

1125 Schulz KJ, DeYoung JH Jr, Seal RR II, Bradley DC (2017) Critical mineral resources of the United States—
1126 Economic and environmental geology and prospects for future supply. Geol Surv Prof Pap 1802:797.
1127 https://doi.org/10.3133/pp1802

1128 Schwarz-Schampera U, Herzig PM (2002) Indium: Geology, Mineralogy and Economics. Springer, Heidelberg

1129 Scotese CR (2009) Late Proterozoic plate tectonics and palaeogeography: A tale of two supercontinents, Rodinia
1130 and Pannotia. In: Craig J, Thurow J, Thusu B, Whitham A, Abutarruma Y (eds) Global Neoproterozoic
1131 Petroleum Systems: The Emerging Potential in North Africa. Geological Society, Special Publications,
1132 London, pp. 326: 67–83

1133 Sempere T (1994) Kimmeridgian? to Paleocene tectonic evolution of Bolivia. In Salfity JA (ed) Cretaceous
1134 tectonics in the Andes. Vieweg Publications, Earth Evolution Sciences Monograph Series, Wiesbaden, pp.
1135 168–212

1136 Sempere T (1995) Phanerozoic evolution of Bolivia and adjacent regions. In: Tankard AJ, Suárez R, Welsink HJ
1137 (eds) Petroleum Basins of South America. AAPG Memoir 62:207–230. https://doi.org/10.1306/M62593C9

1138 Sempere T (2000) Discussion of "Sediment accumulation on top of the Andean orogenic wedge: Oligocene to late
1139 Miocene basins of the eastern Cordillera, southern Bolivia" (Horton, 1998). Geol Soc Am Bull 112:1752-
1140 1755

1141 Sempere T, Hérail G, Oller, Bonhomme MG (1990) Late Oligocene- Early Miocene major tectonic crisis and
1142 related basins in Bolivia. Geology 18:946–949. https://doi.org/10.1130/0091-
1143 7613(1990)018<0946:LOEMMT>2.3.CO;2

1144 Sempere T, Butler RF, Richards DR, Marshall LG, Sharp W, Swisher III CC (1997) Stratigraphy and chronology
1145 of Late Cretaceous – Early Paleogene strata in Bolivia and northwest Argentina. Geol Soc Am Bull
1146 109:709-727. https://doi.org/10.1130/0016-7606(1997)109%3C0709:SACOUC%3E2.3.CO;2

1147 Sempere T, Carlier G, Soler P, Fornari M, Carlotto V, Jacay J, Arispe O, Néraudeau D, Cárdenas J, Rosas S,
1148 Jiménez N (2002) Late Permian–Middle Jurassic lithospheric thinning in Peru and Bolivia, and its bearing
1149 on Andean-age tectonics. Tectonophysics 345:153-181. https://doi.org/10.1016/S0040-1951(01)00211-6

Sempere T, Folguera A, Gerbault M (2008) New insights into the Andean evolution: An introduction to contributions from the 6th ISAG symposium (Barcelona, 2005). Tectonophysics 459:1–13. http://dx.doi.org/10.1016/j.tecto.2008.03.011

Serranti S, Ferrini V, Umberto M, Cabri LJ (2002) Trace-element distribution in cassiterite and sulfides from rubané and massive ores of the Corvo deposit, Portugal. Can Mineral 40:815-835. http://dx.doi.org/10.2113/gscanmin.40.3.815

Sillitoe RH (1972) Relation of metal provinces in western America to subduction of oceanic lithosphere. Geol Soc Am Bull 83:813-818. https://doi.org/10.1130/0016-7606

Sillitoe RH (1976) Andean mineralization: A model for the metallogeny of convergent plate margins: Geol Assoc Can Spec Pap 14:59-100

Sillitoe RH, Halls C, Grant JN (1975) Porphyry tin deposits in Bolivia. Econ Geol 70:913–927. https://doi.org/10.2113/gsecongeo.70.5.913

Sillitoe RH, Steele GB, Thompson JFH, Lang JR (1998) Advanced argillic lithocaps in the Bolivian tin-silver belt. Miner Deposita 33:539–546. https://doi.org/10.1007/s001260050170

Skirrow RG, Huston DL, Mernagh TP, Thorne JP, Dulfer H, Senior AB (2013) Critical commodities for a high-tech world: Australia's potential to supply global demand. Geoscience Australia, Canberra

Slater ET, Kontak DJ, Mcdonald AM, Fayek M (2020) Origin of a multi-stage epithermal Ag-Zn-Pb-Sn deposit: the Miocene Cortaderas breccia body, Pirquitas mine, NW Argentina. Miner Deposita, in press. https://doi.org/10.1007/s00126-020-00976-8

Soler P, Jiménez N (1993) Magmatic constraints upon the evolution of the Bolivian Andes since Late Oligocene times. Extended abstracts, 2nd International Symposium on Andean Geodynamics, Oxford, pp. 447–451

Spikings R, Reitsma MJ, Boekhout F, Mišković A, Ulianov A, Chiaradia M, Gerdes A, Schaltegger U (2016) Characterisation of Triassic rifting in Peru and implications for the early disassembly of western Pangaea. Gondwana Res 35:124–143. https://doi.org/10.1016/j.gr.2016.02.008

Stewart JW, Evernden JF, Snelling NJ (1974) Age Determinations from Andean Peru: A Reconnaissance Survey. Geol Soc Am Bull 85:1107-1116. https://doi.org/10.1130/0016-7606(1974)85%3C1107:ADFAPA%3E2.0.CO;2

Suárez-Soruco R (2000) Compendio de Geología de Bolivia. Servicio Nacional de Geología y Minería, YPFB 18:39-76

Sugaki A, Ueno H, Shimada N, Kitakaze A, Hayashi K, Shima H, Sanjines O, Saavedra M (1981) Geological study on the polymetallic hydrothermal deposits in the Oruro district, Bolivia. Sci Rep Tohoku University, Series III. 15:1–52

Sugaki A, Ueno H, Shimada N, Kusachi I, Kitakaze A, Hayashi K, Kojima S, Sanjines VO (1983) Geological study on the polymetallic ore deposits in the Potosi district, Bolivia. Sci Rep Tohoku University, Series III 15(3):409-460

1185 Sugaki A, Ueno H, Kitakaze A, Hayashi K, Shimada N, Kusachi I, Sanjunes VO (1985) Geological study on the
1186 ore deposits in the La Paz district, Bolivia. Sci Rep Tohoku University, Series III 16(2):132-198

1187 Sugaki A, Kusachi I, Shimada N (1988a) Granite-series and -type of igneous rocks in the Bolivian Andes and their
1188 genetic relation to tin-tungsten mineralization. Min Geol 38:121– 130.
1189 https://doi.org/10.11456/shigenchishitsu1951.38.121

1190 Sugaki A, Kojima S, Shimada N (1988b) Fluid inclusion studies of the polymetallic hydrothermal ore deposits in
1191 Bolivia. Miner Deposita 23:9–15. https://doi.org/10.1007/BF00204221

1192 Sugaki A, Ueno H, Hayashi K (1990) Sulfur isotope reconnaissance of Bolivian hydrothermal deposits. Min Geol
1193 40:299–312. https://doi.org/10.11456/shigenchishitsu1951.40.299

1194 Sugaki A, Shimada N, Ueno H, Kano S (2003) K–Ar ages of tin-polymetallic mineralization in the Oruro mining
1195 district, central Bolivian tin belt. Resour Geol 53:273–282. https://doi.org/10.1111/j.1751-
1196 3928.2003.tb00176.x

1197 Sun SS, McDonough WF (1989) Chemical and isotopic systematics of oceanic basalts: implications for mantle
1198 composition and processes. Geol Soc Lond Spec Pub 42:313-345.
1199 https://doi.org/10.1144/GSL.SP.1989.042.01.19

1200 Taylor RG (1979) Geology of Tin Deposits. Elsevier, The Netherlands

1201 Thormann W (1966) Investigaciones preliminares sobre la geotectónica y metalogénesis de la zona Challapata-
1202 Caxata. Bol Serv Geol Bolivia 7:118

1203 Tindle AG, Breaks FW (1998) Oxide minerals of the Separation Rapids rare-element granitic pegmatite group,
1204 northwestern Ontario. Can Mineral 36:609–635

1205 Tshijik Karumb E (2016) The recovery of indium from mining wastes. PhD thesis, Colorado School of Mines

1206 Torres B, Melgarejo JC, Torró L, Camprubí A, Castillo-Oliver M, Artiaga D, Campeny M, Tauler E, Jiménez-
1207 Franco A, Alfonso P, Arce-Burgoa OR (2019) The Poopó polymetallic epithermal deposit, Bolivia:
1208 mineralogy, genetic constraints, and distribution of critical elements. Minerals 9:472.
1209 https://doi.org/10.3390/min9080472

1210 Torró L, Melgarejo JC, Gemmrich L, Mollinedo D, Cazorla M, Martínez Á, Pujol-Solà N, Farré de Pablo J,
1211 Camprubí A, Artiaga D, Torres B, Alfonso P, Arce-Burgoa OR (2019a) Spatial and temporal controls on
1212 the distribution of indium in xenothermal vein deposits: The Huari Huari district, Potosí, Bolivia. Minerals
1213 9:304. https://doi.org/10.3390/min9050304

1214 Torró L, Cazorla M, Melgarejo JC, Camprubí A, Tarrés M, Gemmrich L, Campeny M, Castillo-Oliver M, Artiaga
1215 D, Torres B, Martínez A, Molliendo D, Alonso P, Arce-Burgoa OR (2019b) Indium mineralization in the
1216 volcanic dome-hosted Ánimas–Chocaya–Siete Suyos polymetallic deposit, Potosí, Bolivia. Minerals 9:604.
1217 https://doi.org/10.3390/min9100604

1218 Turneaure FS (1935) The tin deposits of Llallagua, Bolivia. Econ Geol 30:14–60.
1219 https://doi.org/10.2113/gsecongeo.30.1.14

1220 Turneaure FS (1971) The Bolivian tin-silver province. Econ Geol 66:215–225.
1221 https://doi.org/10.2113/gsecongeo.66.2.215

1222 U.S. Geological Survey (2020) Mineral commodity summaries 2020. U.S. Geological Survey.
1223 https://pubs.usgs.gov/periodicals/mcs2020/mcs2020.pdf. Accessed 19 June 2020

1224 U.S Geological Survey and Servicio Geologico de Bolivia (1992) Geology and mineral resources of the Altiplano
1225 and Cordillera Occidental, Bolivia. Bull US Geol Surv 8:1-365 https://doi.org/10.3133/b1975

1226 Vermeesch P (2018) IsoplotR: A free and open toolbox for geochronology. Geosci Front 9:1479–1493.
1227 https://doi.org/10.1016/j.gsf.2018.04.001

1228 Wise M, Brown C (2011) Chemical composition of coexisting columbite-group minerals and cassiterite from the
1229 Black Mountain pegmatite, Maine. Eur J Mineral. 23:817-828. https://doi.org/10.1127/0935-
1230 1221/2011/0023-2102

1231 Wörner G, Schildgen TF, Reich M (2018a) The Central Andes: Elements of an extreme land. Elements 14:225–
1232 230. https://doi.org/10.2138/gselements.14.4.225

1233 Wörner G, Mamani M, Blum-Oeste M (2018b) Magmatism in the Central Andes. Elements 14:237–244.
1234 https://doi.org/10.2138/gselements.14.4.237

1235 Zhang DL, Peng JT, Hu RZ, Yuan SD, Zheng DS (2011) The closure of U-Pb system in cassiterite and its
1236 reliability for dating. Dizhi Lunping <Geol Rev> 57:549–554 (in Chinese with English abstract)

1237 Zhang R, Lu J, Lehmann B, Li C, Li G, Zhang L, Guo J, Sun W (2017) Combined zircon and cassiterite U–Pb
1238 dating of the Piaotang granite-related tungsten–tin deposit, southern Jiangxi tungsten district, China. Ore
1239 Geol Rev 82:268-284. https://doi.org/10.1016/j.oregeorev.2016.10.039

1240 Zhang S, Zhang R, Lu J, Ma D, Ding T, Gao S, Zhang Q (2019) Neoproterozoic tin mineralization in South China:
1241 Geology and cassiterite U–Pb age of the Baotan tin deposit in northern Guangxi. Miner Deposita 54:1125-
1242 1142. https://doi.org/10.1007/s00126-019-00862-y

1243 Zhao Y, Chen S, Huang Y, Zhao J, Tong Xiang, Chen X (2019) U-Pb Ages, O isotope compositions, Raman
1244 spectrum, and geochemistry of cassiterites from the Xi'ao copper-tin polymetallic deposit in Gejiu District,
1245 Yunnan Province. Minerals 9:212. https://doi.org/10.3390/min9040212

1246 Zoheir B, Lehmann B, Emam A, Radwan A, Zhang R, Bain WM, Steele-MacInnis M, Nolte N (2020) Extreme
1247 fractionation and magmatic–hydrothermal transition in the formation of the Abu Dabbab rare-metal granite,
1248 Eastern Desert, Egypt. Lithos 352–353. Article 105329. https://doi.org/10.1016/j.lithos.2019.105329

1249 **Figure captions**

1250 Fig. 1. (A) Location of the main ore deposits, plutons and volcanic deposits along the Bolivian Tin Belt. Modified
1251 from Mlynarczyk and Williams-Jones (2005). (B) Schematic cross-section model of volcanic- and subvolcanic-
1252 hosted epithermal and xenothermal deposits in the Bolivian Tin Belt (inspired in Pollard et al. 1987 and Heuschmidt
1253 et al. 2002) showing the postulated ideal location of the studied deposits.

Fig. 2. Photomicrographs of representative cassiterite grains for each of the studied Bolivian deposits (reflected light, PPL). (A) Subhedral cassiterite crystals in association with siderite, quartz and basal sections of tourmaline [Kellhuani]. (B) Twinned and fractured euhedral cassiterite crystal in contact with quartz [Viloco]. (C) Fractured subhedral cassiterite crystals with corroded outlines in contact with stannite, sphalerite and pyrrhotite [Viloco]. (D) Massive cassiterite aggregates with abundant secondary porosity in an assemblage of quartz-marcasite [Oruro]. (E) Breccia texture containing small subhedral and anhedral cassiterite grains and pyrite in a micrometric gangue matrix [Oruro]. (F) Subhedral to anhedral cassiterite grains in contact with sphalerite and pyrite-marcasite after pyrrhotite showing "bird's eye" textures [Poopó]. (G) Massive euhedral to subhedral fractured cassiterite grains [Huanuni]. (H) Massive, twinned cassiterite crystals in an assemblage of quartz and tourmaline [Llallagua]. (I) Breccia-type mineralization with subhedral cassiterite grains along with quartz, pyrite, galena, sphalerite and late siderite [Colquechaca]. (J) Leather-shaped radial aggregates of cassiterite surrounded by massive sphalerite [Colquechaca]. (K) Complex sulfide and sulfosalt assemblage along with corroded and twinned cassiterite crystals [Huari Huari]. (L) Garland-like arrangement of cassiterite, sulfides and sulfosalts wrapping a euhedral hexagonal quartz crystal [Ánimas - Chocaya - Siete Suyos]. Abbreviations: Ara = aramayoite; Cst = cassiterite; Cpy = chalcopyrite; Gn = galena; Mcs = marcasite; Mia = miargyrite; Osc = oscarkempffite; Pyr = pyrargyrite; Po = pyrrhotite; Py = pyrite; Qz = quartz; Sid = siderite; Sl = sphalerite; Stn = stannite; Ttd = tetrahedrite-group; Turm = tourmaline.

Fig. 3. Selected box plots showing element concentrations in cassiterite from the Bolivian Tin Belt (LA-ICP-SF-MS data).

Fig. 4. Correlation binary plots for cassiterite from the Bolivian tin belt. Bibliographic data is shown for comparison. Granite-hosted and granite cupolas: Moore and Howie (1979), Lentz and McAllister (1990), Plimer et al. (1991), Murciego et al. (1997), Gorelikova et al. (2004, 2006), Abdalla et al. (2008), Neiva (2008), Pavlova et al. (2015), Lerouge et al. (2017), Nascimento and Souza (2017), Zhang et al. (2017), Chen et al. (2019), Cheng et al. (2019), Fuchsloch et al. (2019), Zoheir et al. (2019), Mao et al. (2020). Greisen-type: Plimer et al. (1991), Pavlova et al. (2015), Chen et al. (2019), Cheng et al. (2019), Fuchsloch et al. (2019), Hulsbosch and Muchez (2019). Migmatitic-related: Murciego et al. (1997), Jiang et al. (2004). Pegmatite: Murciego et al. (1997), Plimer et al. (1991), Wise and Brown. (2011), Hulsbosch and Muchez (2019), Kendall-Langley et al. (2019). Xenothermal and epithermal environment: Murciego et al. (1997), Pavlova et al. (2015), Guo et al. (2018), Cheng et al. (2019), Zhao et al. (2019). Skarn: Cheng et al. (2019). VMS: Serranti et al. (2002).

Fig. 5. Chondrite-normalized REE spider diagrams for Bolivian Tin Belt cassiterite represented as individual analyses (A) and as average values for each deposit/district (B). Bibliographic data are shown for comparison. Granite-hosted and granite cupolas: Plimer et al. (1991), Zoheir et al. (2019). Greisen-type: Plimer et al. (1991). Migmatitic-related: Jiang et al. (2004).

Fig. 6. Tera-Wasserburg U-Pb concordia plots for cassiterite from the Kellhuani, Viloco, Huanuni and Llallagua deposits.

Fig. 7. Triassic to recent geochronologic chart of the Bolivian Tin Belt, including the new U-Pb cassiterite data presented here. Data are ordered from north to south of the Bolivian Tin Belt. Circled numbers correspond to the following references: 1) Ahfeld and Brainsa (1960); 2) Ahfeld and Schneider-Scherbina (1964); 3) Clark and Farrar (1973); 4) Clark et al. (1983); 5) Clark et al. (2000); 6) Cordani (1967); 7) Cordani et al. (2019); 8) Cunningham et al. (1996); 9) Everden (1961); 10) Everden et al. (1997); 11) Gillis et al. (2006); 12) Grant et al. (1979); 13) Kempe et al. (2008); 14) Kontak and Clark (2002); 15) Kontak et al. (1987); 16) McBride et al. (1983); 17) Redwood and Macintyre (1989); 18) Revollo (1967); 19) Rivas and Carrasco (1968); 20) Thormann (1966); 21) Farrar et al. (1990).

Table captions

Table 1. Average REE concentrations for Bolivian Tin Belt cassiterite and bibliographic data: Granite-hosted and granite cupolas: Plimer et al. (1991), Zoheir et al. (2019). Greisen-type: Plimer et al. (1991). Migmatitic-related: Jiang et al. (2004). REE division after Samson and Wood (2004); LREE: La-Sm; MREE: Eu-Dy; HREE: Ho-Lu.

Table 2. Summary of the concentrations of Nb, Ta, In, Ge and Ga in cassiterite grains from the Bolivian tin belt. Bibliographic data are shown for comparison (references as in Fig. 4).

Table 3. Maximum reported concentrations of In, Ge, Ga, Nb and Ta in ore minerals and concentrates from deposits in the Bolivian Tin Belt.

Supplementary material

Supplementary Table S1. EPMA data for spot analyses of cassiterite grains from the Bolivian Tin Belt.

Supplementary Table S2. LA-ICP-MS combined trace element and U-Pb isotopic analyses on cassiterite - Metadata.

Supplementary Table S3. Trace-element LA-ICP-MS data for spot analyses of cassiterite grains from the Bolivian Tin Belt.

Supplementary Table S4. U-Pb LA-ICP-MS data for spot analyses of cassiterite grains from the Bolivian Tin Belt.

Supplementary Figure S1. Representative downhole LA-ICP-MS spectra for elements at concentrations >L.O.D. in studied cassiterite from the Bolivian tin belt.

Supplementary Figure S2. Box plots showing element concentrations in cassiterite from the Bolivian Tin Belt (LA-ICP-SF-MS data).

Supplementary Figure S3. Ternary diagrams representing cassiterite analyses from Bolivian Tin Belt and bibliographic data. The centered ternary plot (C) is used to accentuate compositional variation in unbalanced compositional data by centering the data-set on its average and visualizing the transformed data with a standard ternary balance scheme. References given in Fig. 4 caption.

Table 1

	ppm	∑REE	∑LREE	∑MREE	∑HREE	$\sum LREE/MREE_{CN}$	$\sum LREE/HREE_{CN}$	$\sum MREE/HREE_{CN}$
Kellhuani (n=30)	*Max.*	38.3	13.2	21.3	3.79	0.4	1.6	4.5
	Min.	0.513	0.168	0.266	0.046	0.3	0.6	1.7
	IQR	6.18-2.19	2.28-0.766	3.32-1.14	0.706-0.216	0.4-0.3	1.4-1.0	4.1-2.7
Viloco (n=81)	*Max.*	35.5	13.5	19.6	2.71	0.4	1.9	5.0
	Min.	0.351	0.124	0.190	0.0367	0.3	0.3	0.8
	IQR	4.42-1.61	1.55-0.562	2.21-0.865	0.483-0.181	0.4-0.4	1.5-1.0	4.2-2.7
San José - Itos (Oruro) (n=22)	*Max.*	13.9	5.28	7.41	1.18	0.6	2.4	5.3
	Min.	0.498	0.182	0.218	0.0375	0.4	0.9	2.6
	IQR	3.58-1.55	1.30-0.621	1.96-0.825	0.315-0.137	0.4-0.4	1.7-1.5	4.5-4.0
Poopó (n=9)	*Max.*	5.50	2.00	3.04	0.467	0.4	1.7	4.7
	Min.	0.384	0.142	0.209	0.0326	0.3	1.4	4.1
	IQR	3.26-1.98	1.16-0.711	1.83-1.10	0.272-0.178	0.4-0.4	1.6-1.5	4.6-4.4
Huanuni (n=59)	*Max.*	14.6	5.30	8.12	1.21	0.4	1.9	5.1
	Min.	0.214	0.0791	0.117	0.0184	0.3	1.5	3.9
	IQR	2.58-1.90	0.977-0.698	1.41-1.04	0.216-0.153	0.4-0.4	1.7-1.6	4.7-4.4
Llallagua (n=13)	*Max.*	11.7	4.03	6.65	0.991	0.4	1.7	4.8
	Min.	0.452	0.164	0.251	0.0368	0.3	1.2	3.3
	IQR	3.99-2.30	1.41-0.832	2.21-1.24	0.373-0.198	0.4-0.3	1.6-1.5	4.4-4.2
Colquechaca (n=5)	*Max.*	2.57	0.984	1.36	0.253	0.4	1.8	4.5
	Min.	1.73	0.661	0.921	0.144	0.4	1.5	3.6
	IQR	2.47-2.12	0.907-0.784	1.33-1.14	0.203-0.197	0.4-0.4	1.7-1.5	4.5-3.9
Huari Huari (n=9)	*Max.*	21.3	8.01	11.5	1.73	0.4	1.9	5.0
	Min.	1.74	0.644	0.954	0.145	0.3	1.3	3.9
	IQR	3.76-1.99	1.38-0.715	2.06-1.10	0.317-0.186	0.4-0.4	1.6-1.5	4.6-4.0
Ánimas - Chocaya - Siete Suyos (n=17)	*Max.*	4.66	1.68	2.56	0.421	0.4	1.6	4.8
	Min.	0.0636	0.0234	0.0342	0.00590	0.3	1.5	4.1
	IQR	2.12-1.44	0.784-0.543	1.14-0.769	0.197-0.125	0.4-0.4	1.6-1.5	4.4-4.2
Granite hosted and granite cupolas (n=28)	*Max.*	447	356	48.0	42.8	7.9	80.9	10.5
	Min.	0.658	0.0930	0.0850	0.260	0.1	0.02	0.1
	IQR	164-1.37	144-0.187	11.2-0.132	5.27-0.817	3.9-0.3	3.0-0.05	0.8-0.1
Greisen-type (n=2)	*Max.*	12.8	10.2	1.10	1.54	4.4	1.7	0.4
	Min.	2.19	0.490	0.710	0.990	0.4	0.1	0.4
Migmatitic-related (n=1)		1.83	1.10	0.350	0.380	1.3	0.7	0.5

Table 2

		Nb (ppm)	Ta (ppm)	In (ppm)	Ge (ppm)	Ga (ppm)
Kellhuani (n=30)	*Max.*	2008	2.29	95.7	2.25	20.4
	Min.	0.0626	0.00324	0.700	B.D.L.	0.400
	IQR	60.8-2.26	0.639-0.0403	30.9-2.15	1.25-0.499	3.11-0.932
Viloco (n=81)	*Max.*	1011	114	268	13.5	42.5
	Min.	B.D.L.	0.00285	0.500	B.D.L.	0.422
	IQR	6.19-0.0515	0.135-0.0138	63.4-10.0	1.85-0.499	5.43-1.59
San José - Itos (Oruro) (n=22)	*Max.*	11.3	0.575	1414	21.9	1314
	Min.	0.0605	0.00806	7.70	0.573	13.2
	IQR	3.76-0.417	0.075-0.0259	801-31.8	10.1-1.58	377-71
Poopó (n=9)	*Max.*	0.0370	0.0411	8.30	10.6	49.7
	Min.	0.00649	0.00254	1.60	0.715	18.3
	IQR	0.027-0.0126	0.0196-0.0133	4.7-3	6.45-2.97	43.3-27.3
Huanuni (n=59)	*Max.*	43.0	0.929	260	6.36	396
	Min.	B.D.L.	0.00139	1.40	0.107	8.87
	IQR	0.488-0.0377	0.025-0.011	122-20.3	3.79-1.47	217-52.9
Llallagua (n=13)	*Max.*	63.8	1.06	44.2	3.93	78.6
	Min.	0.0167	0.0106	1.60	0.508	7.01
	IQR	18.5-0.989	0.185-0.0143	25-6.5	3.48-2.2	53.1-23.0
Colquechaca (n=5)	*Max.*	1.06	0.0294	104	7.34	503
	Min.	0.0194	0.0162	1.70	2.23	23.4
	IQR	0.611-0.022	0.0289-0.0226	95.2-1.7	6.37-2.78	438-53.5
Huari Huari (n=9)	*Max.*	6.05	0.253	1041	8.32	916
	Min.	0.00684	0.0113	11.3	0.913	105
	IQR	2.58-0.034	0.0872-0.0267	889-96.9	4.79-2.89	690-150
Ánimas - Chocaya - Siete Suyos (n=17)	*Max.*	0.689	0.0299	996	33.6	7437
	Min.	B.D.L.	0.000390	56.7	0.219	2.31
	IQR	0.059-0.00971	0.0165-0.00873	582-174	7.81-3.23	292-53.1
Granite-hosted and granite cupolas (n=392)	*Max.*	26800	306700	800	1.17	400
	Min.	B.D.L.	B.D.L.	B.D.L.	0.03	B.D.L.
	IQR	3389-100	5078-100	304-2.50	0.59-0.263	19.9-5.00
Greisen-type (n=103)	*Max.*	26800	103300	160	-	22.9
	Min.	0.07	B.D.L.	0.02	-	0.68
	IQR	2400-308	6311-170	2.30-0.195	-	9.00-2.74
Migmatitic-related (n=6)	*Max.*	6400	100	-	-	-
	Min.	0.17	0.07	-	-	-
	IQR	2225-150	100-25.1	-	-	-
Pegmatite (n=177)	*Max.*	28500	32000	0.02	24997	4580
	Min.	B.D.L.	B.D.L.	0.02	B.D.L.	B.D.L.
	IQR	2780-175	4088-0.55	-	361-13.0	593-115
Skarn (n=21)	*Max.*	626	248	-	-	27.5
	Min.	5.51	0.05	-	-	1
	IQR	146-25.4	12.9-1.42	-	-	8.74-1.78
VMS (n=2)	*Max.*	-	53	309	-	-
	Min.	-	45	284	-	-
	IQR	-	51.0-47.0	303-290	-	-
Xenothermal and epithermal environment (n=48)	*Max.*	13316	3760	1508	-	149
	Min.	B.D.L.	B.D.L.	3.88	-	0.22
	IQR	172-0.12	31.5-0.01	358-5.00	-	21.3-2.06

Table 3

Reference	Deposit	Method	Sample type	In (ppm)	Ge (ppm)	Ga (ppm)
Ishihara et al. (2011)	Cerro Rico de Potosí	ICP-MS	Sphalerite	5740		69
Ishihara et al. (2011)	Pailaviri	ICP-MS	Composite ore	43		28
Ishihara et al. (2011)	San Jacinto	ICP-MS	Composite ore	292		24
Ishihara et al. (2011)	Huari Huari	ICP-MS	Composite ores	3080		148
Ishihara et al. (2011)	Reserva	ICP-MS	Zn concentrate	553		14
Ishihara et al. (2011)	San Lorenzo	ICP-MS	Zn concentrate	1080		9
Ishihara et al. (2011)	Tuntoco	ICP-MS	Composite ore	100		125
Ishihara et al. (2011)	Porco	ICP-MS	Sphalerite	821		138
Ishihara et al. (2011)	Bolívar	ICP-MS	Breccia Ore	2730		284
Ishihara et al. (2011)	Colquiri	ICP-MS	Ore	393		88
Ishihara et al. (2011)	Siete Suyos - Ánimas	ICP-MS	Composite Ore	2240		312
Ishihara et al. (2011)	Ánimas	ICP-MS	Composite Ore	2510		210
Ishihara et al. (2011)	Chorolque	ICP-MS	Composite Ore	1		32
Ishihara et al. (2011)	Tatasi	ICP-MS	Composite Ore	630		24
Ishihara et al. (2011)	San Vicente	ICP-MS	Sphalerite ore	1290		133
Ishihara et al. (2011)	Pirquitas (Argentina)	ICP-MS	Composite ore	1160		567
Ishihara et al. (2011)	San Cristóbal	ICP-MS	Zn concentrate	11		17
Ishihara et al. (2011)	Cerro Rico de Potosí	EPMA	Sphalerite	12700		
Ishihara et al. (2011)	Cerro Rico de Potosí	EPMA	Petrukite	48600		
Ishihara et al. (2011)	Bolívar	ICP-MS	Zn concentrate	584		
Ishihara et al. (2011)	Colquiri	ICP-MS	Zn concentrate	213		
Ishihara et al. (2011)	Porco	ICP-MS	Zn concentrate	499		
Ishihara et al. (2011)	Huari Huari	ICP-MS	Zn concentrate	3080		
Ishihara et al. (2011)	Cerro Rico de Potosí	ICP-MS	Zn concentrate	1199		
Ishihara et al. (2011)	San Lorenzo	ICP-MS	Zn concentrate	1080		
Ishihara et al. (2011)	Bolívar	ICP-MS	Zn concentrate	584		
Ishihara et al. (2011)	Reserva	ICP-MS	Zn concentrate	553		
Ishihara et al. (2011)	Porco	ICP-MS	Zn concentrate	499		
Ishihara et al. (2011)	Colquiri	ICP-MS	Zn concentrate	213		
Ishihara et al. (2011b)	San Cristóbal	ICP-MS	Zn concentrate	10.7		
Artiaga et al. (2013)	Viloco	EPMA	Stannite	20400		
Artiaga et al. (2013)	Viloco	EPMA	Sphalerite	2000		
Murakami and Ishihara (2013)	Cerro Rico de Potosí	EPMA	Sphalerite	95900		
Murakami and Ishihara (2013)	Huari Huari	EPMA	Sphalerite	182200		
Murakami and Ishihara (2013)	Bolívar	EPMA	Sphalerite	6900		
Murakami and Ishihara (2013)	Porco	EPMA	Sphalerite	3900		
Murakami and Ishihara (2013)	Cerro Rico de Potosí	fsLA-ICPMS	Sphalerite	430		
Murakami and Ishihara (2013)	Huari Huari	fsLA-ICPMS	Sphalerite	3450		116
Murakami and Ishihara (2013)	Bolívar	fsLA-ICPMS	Sphalerite	2290		249
Murakami and Ishihara (2013)	Porco	fsLA-ICPMS	Sphalerite	20		35
Murakami and Ishihara (2013)	Cerro Rico de Potosí	fsLA-ICPMS	Miargyrite	4		not detected
Murakami and Ishihara (2013)	Huari Huari	fsLA-ICPMS	Jamesonite	624		not detected
Jiménez-Franco et al. (2018)	Santa Fe	ICP-MS	Porphyry stock	2.5		47
Jiménez-Franco et al. (2018)	Santa Fe	ICP-MS	Dome	1.6		5
Jiménez-Franco et al. (2018)	Santa Fe	ICP-MS	Dike	2.2		9
Jiménez-Franco et al. (2018)	Santa Fe	ICP-MS	Host rock	1		15
Jiménez-Franco et al. (2018)	Morococala (Santa Fe)	ICP-MS	Concentrate	200		35
Jiménez-Franco et al. (2018)	Japo (Santa Fe)	ICP-MS	Concentrate	200		21
Jiménez-Franco et al. (2018)	Santa Fe	EPMA	Sphalerite	300		
Jiménez-Franco et al. (2018)	Morococala (Santa Fe)	EPMA	Sphalerite	1700		
Jiménez-Franco et al. (2018)	Japo (Santa Fe)	EPMA	Stannite	2000		
Jiménez-Franco et al. (2018)	Morococala (Santa Fe)	EPMA	Stannite	4500		
Jiménez-Franco et al. (2018)	Japo (Santa Fe)	EPMA	Sakuraiite	1400		
Jiménez-Franco et al. (2018)	Morococala (Santa Fe)	EPMA	Sakuraiite	16800		
Jiménez-Franco et al. (2018)	Japo (Santa Fe)	EPMA	Kërsterite	1400		
Cacho et al. (2019)	Huanuni	EPMA	Sphalerite	8800		
Cacho et al. (2019)	Huanuni	EPMA + LA-ICPMS	Stannite	3300	1300	123
Torres et al. (2019)	Poopó	EPMA + LA-ICPMS	Sphalerite	10500		1360
Torres et al. (2019)	Poopó	EPMA + LA-ICPMS	Stannite	11100		199
Torres et al. (2019)	Poopó	EPMA + LA-ICPMS	Rhodostannite	6070	2100	441
Torres et al. (2019)	Poopó	EPMA + LA-ICPMS	Teallite	10800		108
Torres et al. (2019)	Poopó	EPMA	Franckeite		1600	
Torró et al. (2019a)	Huari Huari	EPMA	Sphalerite	34900	800	6400
Torró et al. (2019a)	Huari Huari	EPMA	Stannite	26400	not detected	1400
Torró et al. (2019a)	Huari Huari	EPMA	Jamesonite	1400		100
Torró et al. (2019b)	Ánimas - Chocaya - Siete Suyos	EPMA	Sphalerite	96600	700	
Torró et al. (2019b)	Ánimas - Chocaya - Siete Suyos	EPMA	Stannite	41100	1400	
Pring et al. (2020)	Ánimas - Chocaya	LA-ICP-MS	Wurtzite	150		
Pring et al. (2020)	Ánimas - Chocaya	LA-ICP-MS	Sphalerite	600		

Figure 1

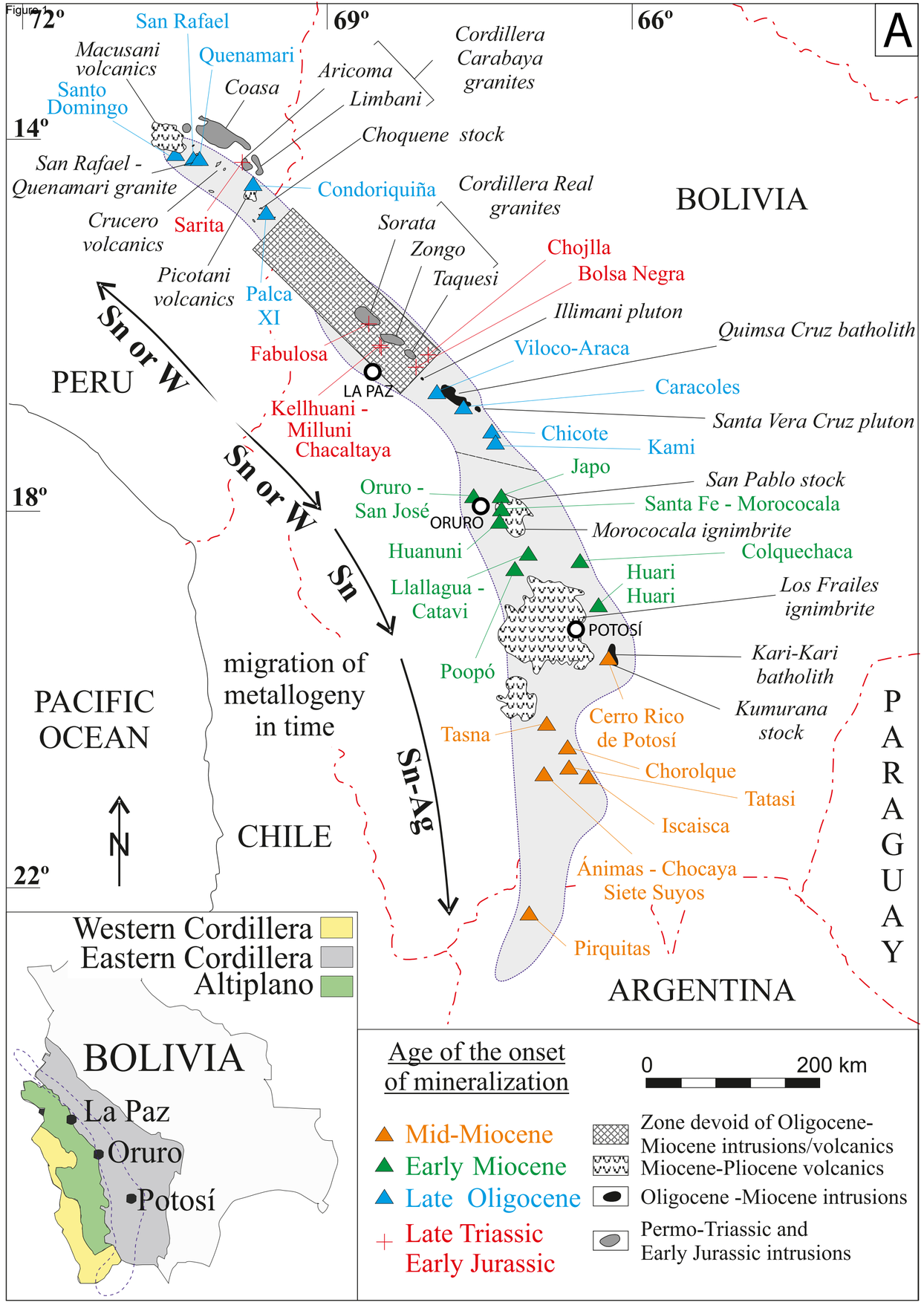
A
72º
69º
66º
14º
18º
22º
San Rafael
Macusani volcanics
Quenamari
Coasa
Aricoma
Limbani
Cordillera Carabaya granites
Santo Domingo
Choquene stock
San Rafael - Quenamari granite
Condoriquiña
Cordillera Real granites
BOLIVIA
Crucero volcanics
Sarita
Sorata
Zongo
Taquesi
Chojlla
Bolsa Negra
Picotani volcanics
Palca
XI
Illimani pluton
Quimsa Cruz batholith
Sn or W
PERU
Fabulosa
LA PAZ
Viloco-Araca
Caracoles
Kellhuani - Milluni Chacaltaya
Santa Vera Cruz pluton
Chicote
Kami
Japo
Sn or W
Oruro - San José
ORURO
San Pablo stock
Santa Fe - Morococala
Morococala ignimbrite
Huanuni
Colquechaca
Sn
Llallagua - Catavi
Huari Huari
Los Frailes ignimbrite
POTOSÍ
Kari-Kari batholith
Poopó
Kumurana stock
migration of metallogeny in time
Cerro Rico de Potosí
Tasna
Chorolque
Tatasi
PACIFIC OCEAN
Sn-Ag
Iscaisca
Ánimas - Chocaya Siete Suyos
CHILE
Pirquitas
PARAGUAY
ARGENTINA
N
Western Cordillera
Eastern Cordillera
Altiplano
BOLIVIA
La Paz
Oruro
Potosí
Age of the onset of mineralization
Mid-Miocene
Early Miocene
Late Oligocene
Late Triassic Early Jurassic
0
200 km
Zone devoid of Oligocene-Miocene intrusions/volcanics
Miocene-Pliocene volcanics
Oligocene -Miocene intrusions
Permo-Triassic and Early Jurassic intrusions

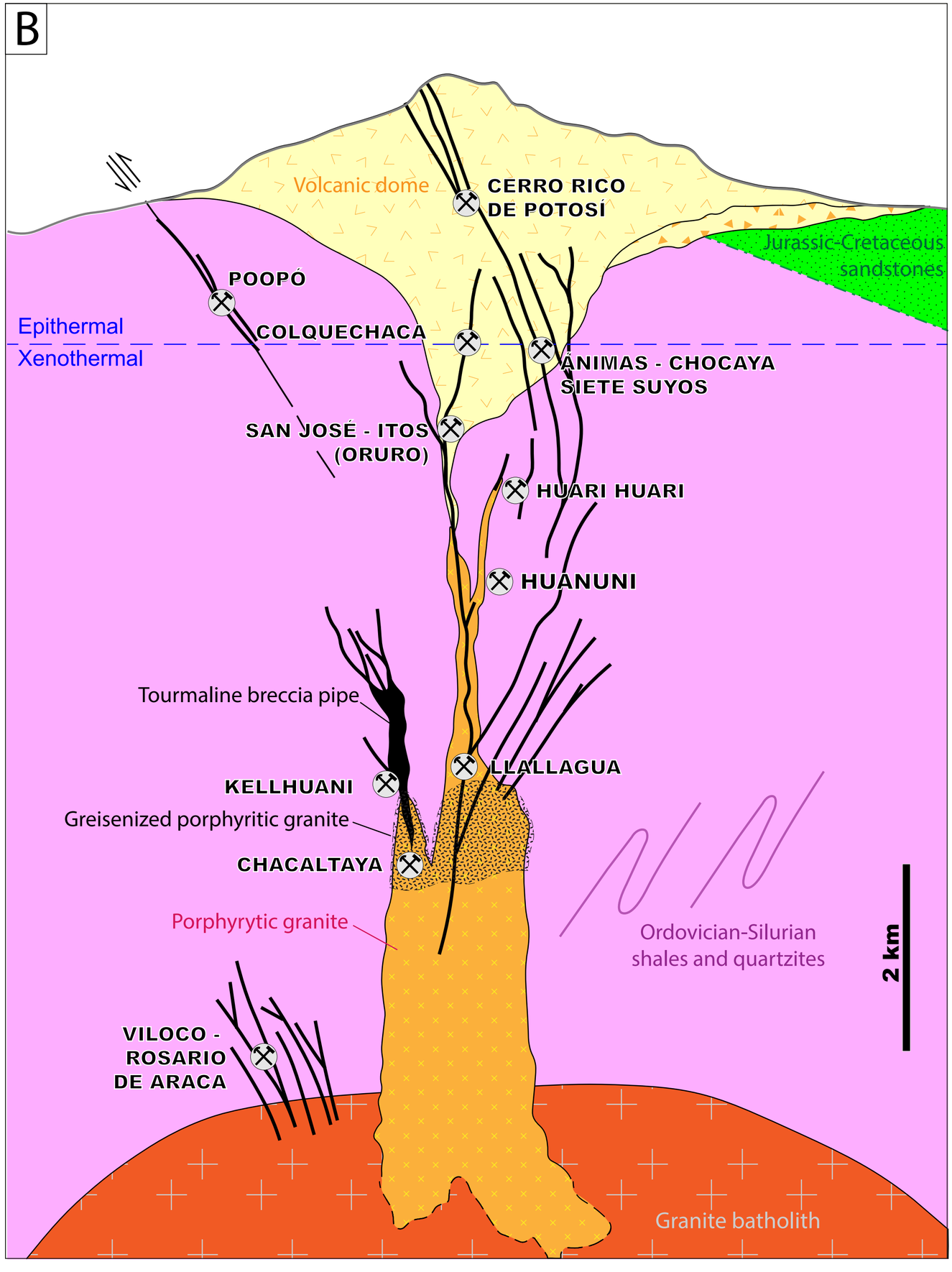
B
Volcanic dome
CERRO RICO DE POTOSÍ
Jurassic-Cretaceous sandstones
POOPÓ
Epithermal
Xenothermal
COLQUECHACA
ÁNIMAS - CHOCAYA
SIETE SUYOS
SAN JOSÉ - ITOS (ORURO)
HUARI HUARI
HUANUNI
Tourmaline breccia pipe
LLALLAGUA
KELLHUANI
Greisenized porphyritic granite
CHACALTAYA
Porphyrytic granite
Ordovician-Silurian shales and quartzites
2 km
VILOCO - ROSARIO DE ARACA
Granite batholith

Figure 2

Click here to access/download;Figure;Figure_2_Micro.jpg

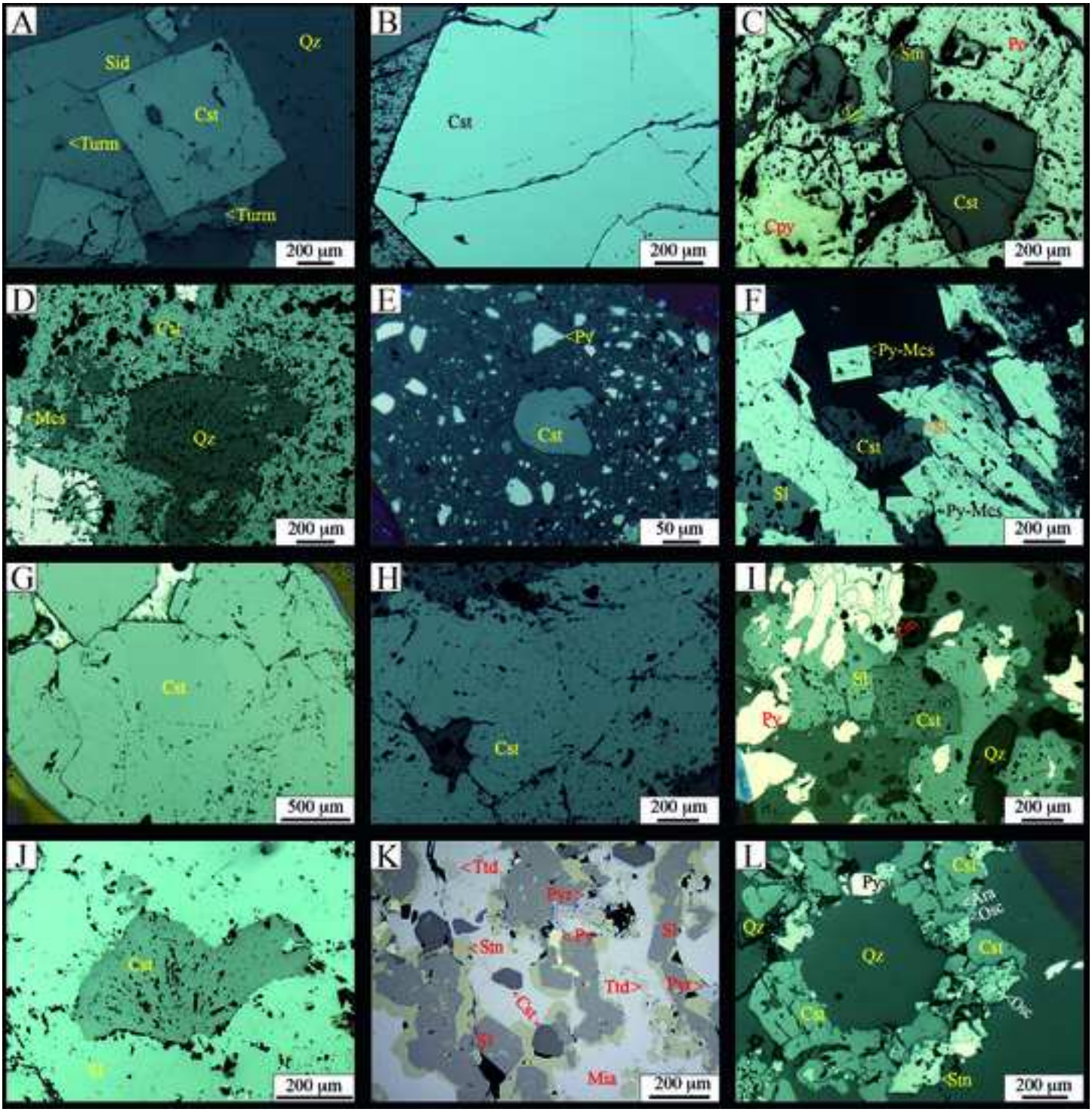

Figure 3

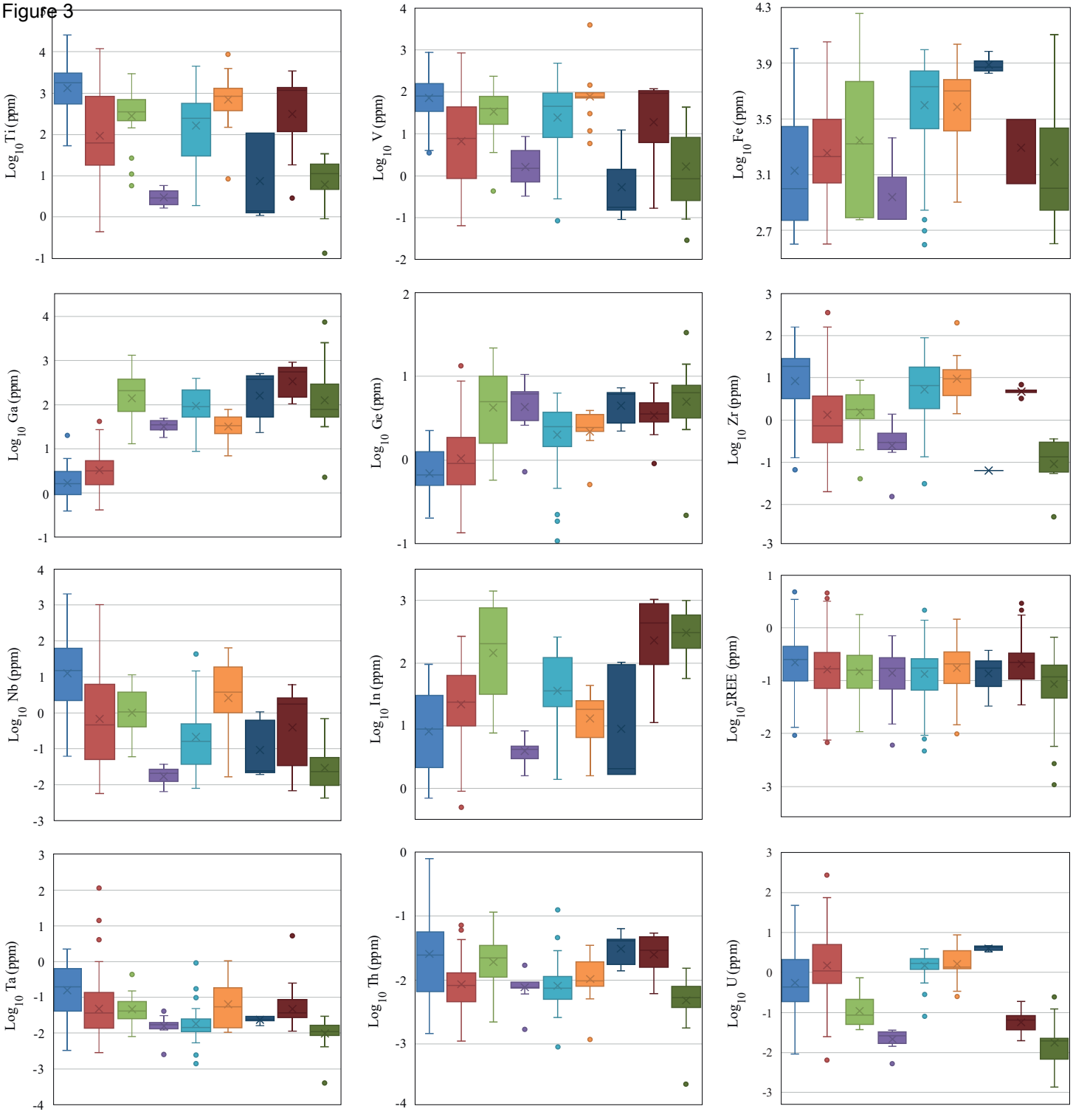
Log10 Ti (ppm)
Log10 V (ppm)
Log10 Fe (ppm)
Log10 Ga (ppm)
Log10 Ge (ppm)
Log10 Zr (ppm)
Log10 Nb (ppm)
Log10 In (ppm)
Log10 ΣREE (ppm)
Log10 Ta (ppm)
Log10 Th (ppm)
Log10 U (ppm)
Mine district
Kellhuani
Poopó
Colquechaca
Viloco
Huanuni
Huari Huari
San José - Itos (Oruro)
Llallagua
Ánimas - Chocaya - Siete Suyos
Interquartile Range (IQR)
Range within 1.5 IQR
Median line
Mean
Outliers

Figure 4

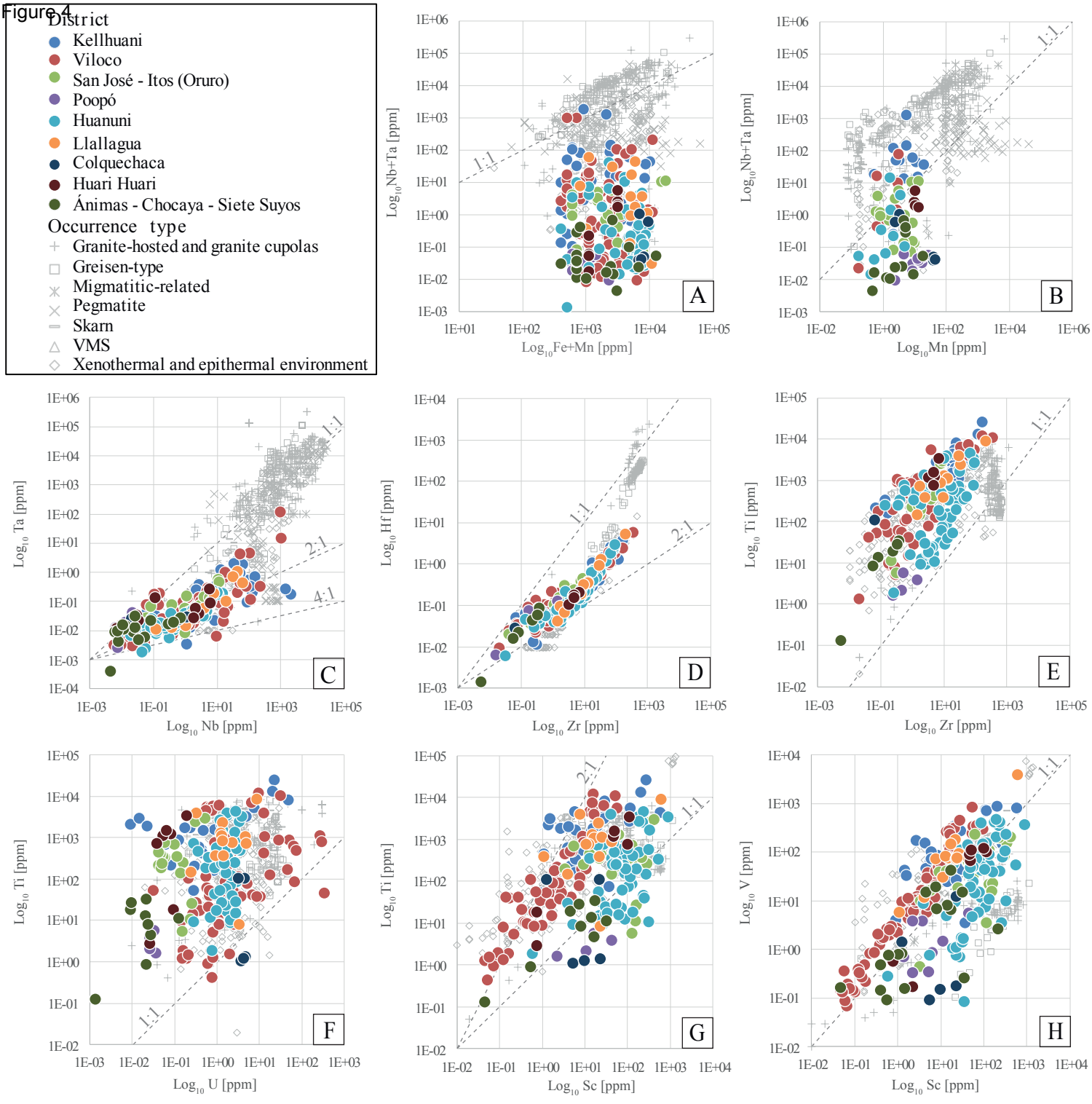
District
Kellhuani
Viloco
San José - Itos (Oruro)
Poopó
Huanuni
Llallagua
Colquechaca
Huari Huari
Ánimas - Chocaya - Siete Suyos
Occurrence type
Granite-hosted and granite cupolas
Greisen-type
Migmatitic-related
Pegmatite
Skarn
VMS
Xenothermal and epithermal environment
A
Log10Nb+Ta [ppm]
Log10Fe+Mn [ppm]
1:1
B
Log10Nb+Ta [ppm]
Log10Mn [ppm]
1:1
C
Log10 Ta [ppm]
Log10 Nb [ppm]
1:1
2:1
4:1
D
Log10 Hf [ppm]
Log10 Zr [ppm]
1:1
2:1
E
Log10 Ti [ppm]
Log10 Zr [ppm]
1:1
F
Log10 Ti [ppm]
Log10 U [ppm]
1:1
G
Log10 Ti [ppm]
Log10 Sc [ppm]
2:1
1:1
H
Log10 V [ppm]
Log10 Sc [ppm]
1:1

Figure 5

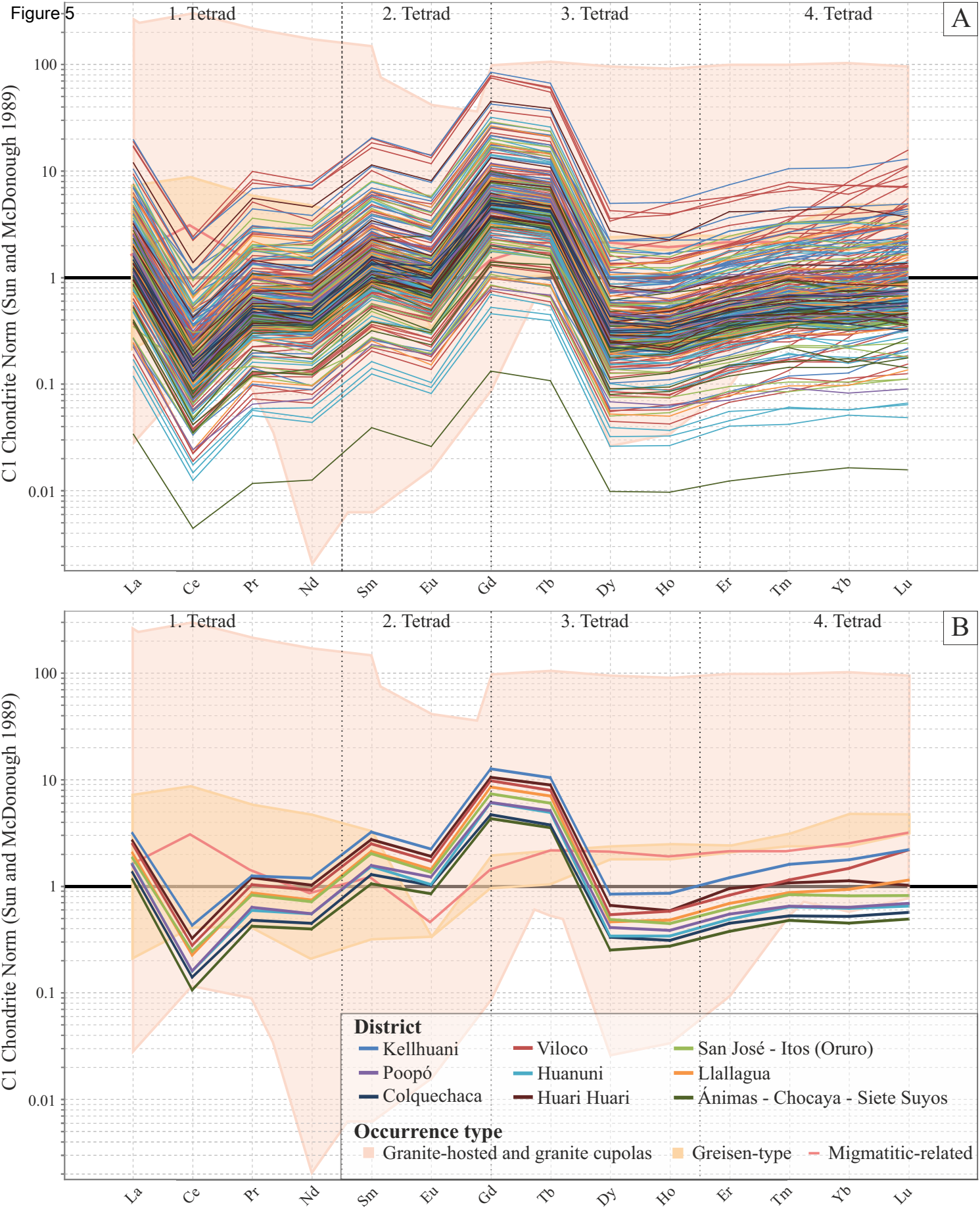
A
1. Tetrad
2. Tetrad
3. Tetrad
4. Tetrad
C1 Chondrite Norm (Sun and McDonough 1989)
100
10
1
0.1
0.01
La
Ce
Pr
Nd
Sm
Eu
Gd
Tb
Dy
Ho
Er
Tm
Yb
Lu
B
1. Tetrad
2. Tetrad
3. Tetrad
4. Tetrad
C1 Chondrite Norm (Sun and McDonough 1989)
100
10
1
0.1
0.01
La
Ce
Pr
Nd
Sm
Eu
Gd
Tb
Dy
Ho
Er
Tm
Yb
Lu
District
Kellhuani
Viloco
San José - Itos (Oruro)
Poopó
Huanuni
Llallagua
Colquechaca
Huari Huari
Ánimas - Chocaya - Siete Suyos
Occurrence type
Granite-hosted and granite cupolas
Greisen-type
Migmatitic-related

Figure 6

Click here to access/download;Figure;Figure_6_U-Pb.jpg

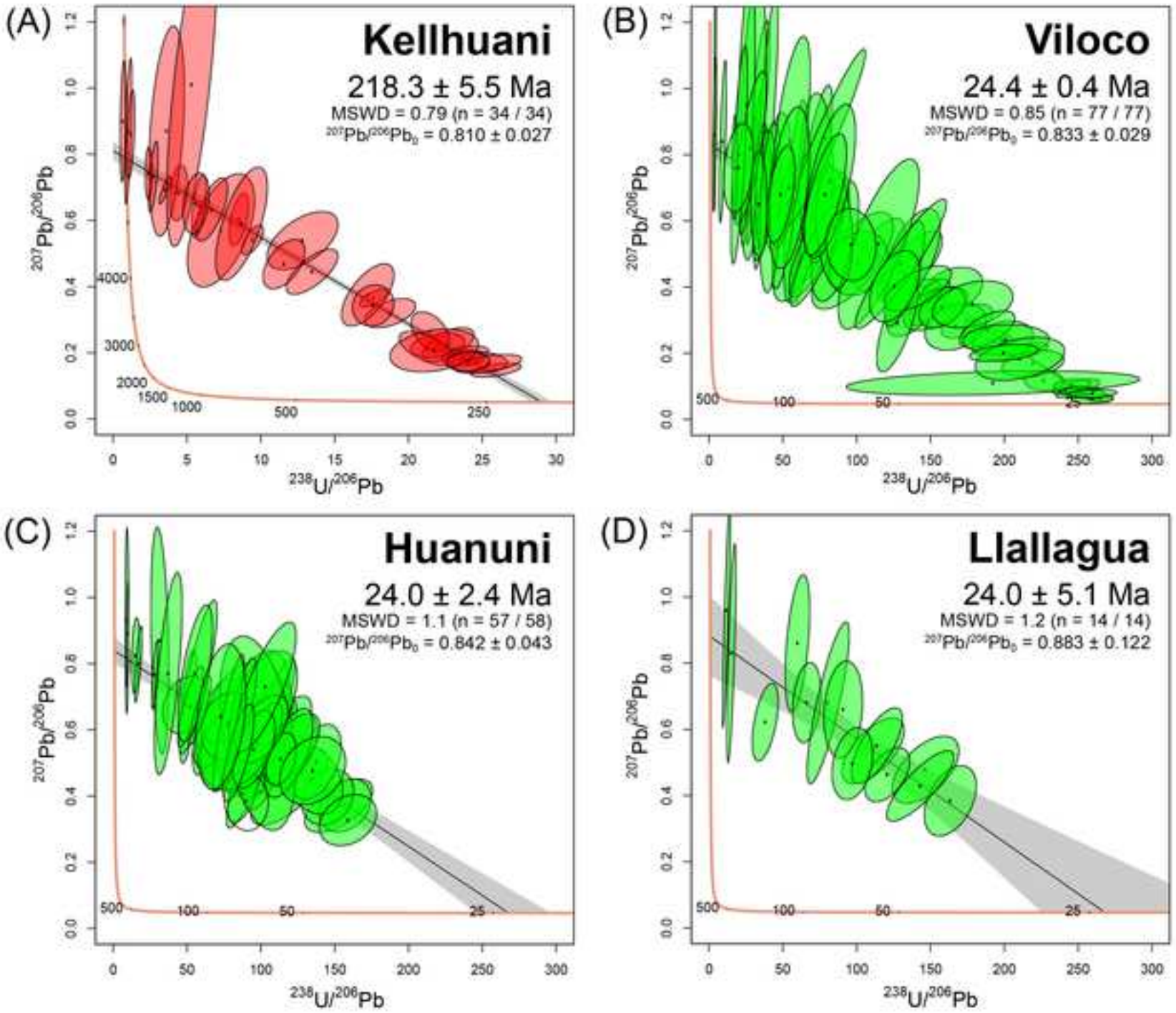

Figure 7_1

Click here to access/download;Figure;Figure_7_Geochronology chart 1-01.jpg

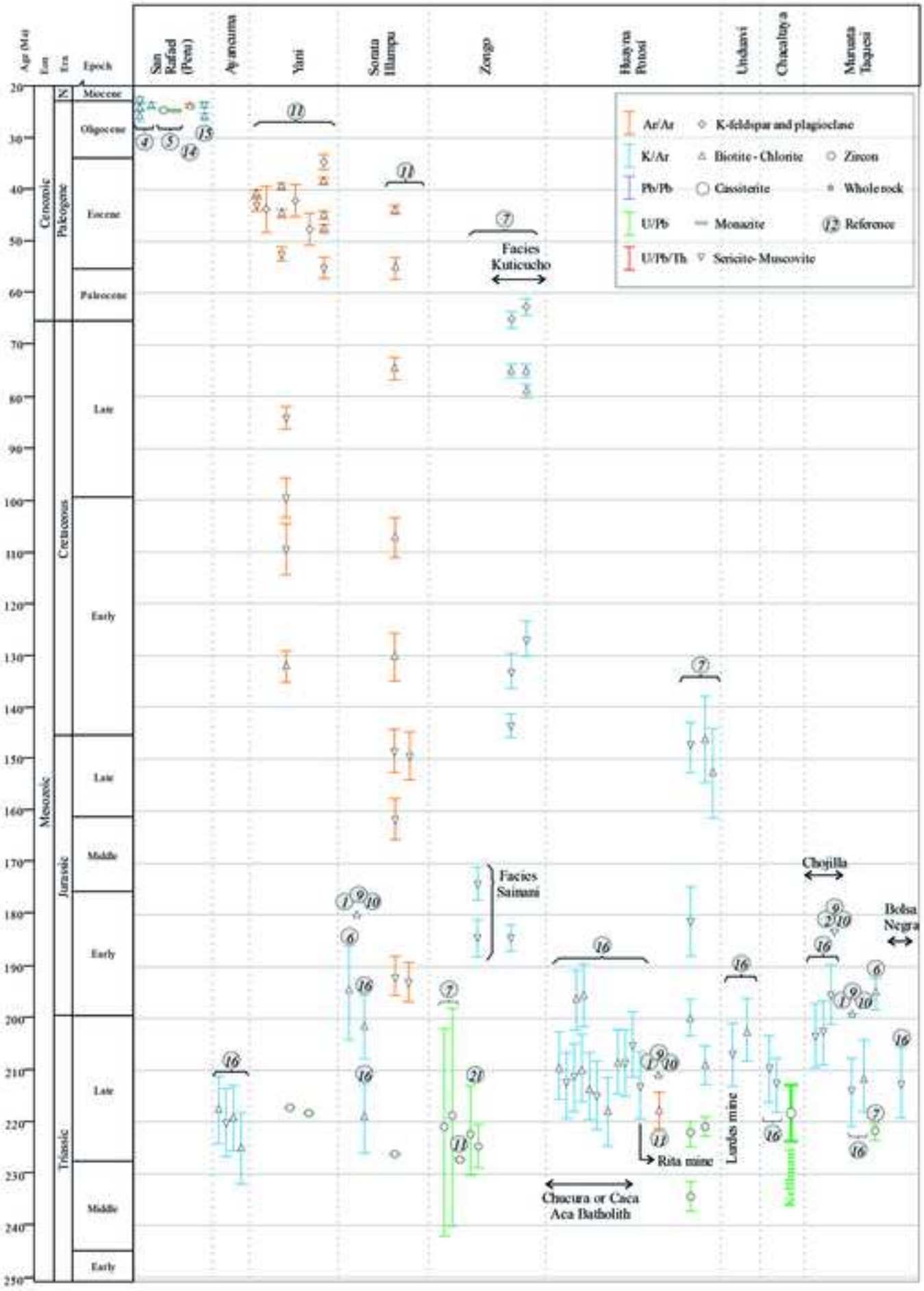

Figure 7_2

Click here to access/download;Figure;Figure_7_Geochronology chart 2-01.jpg

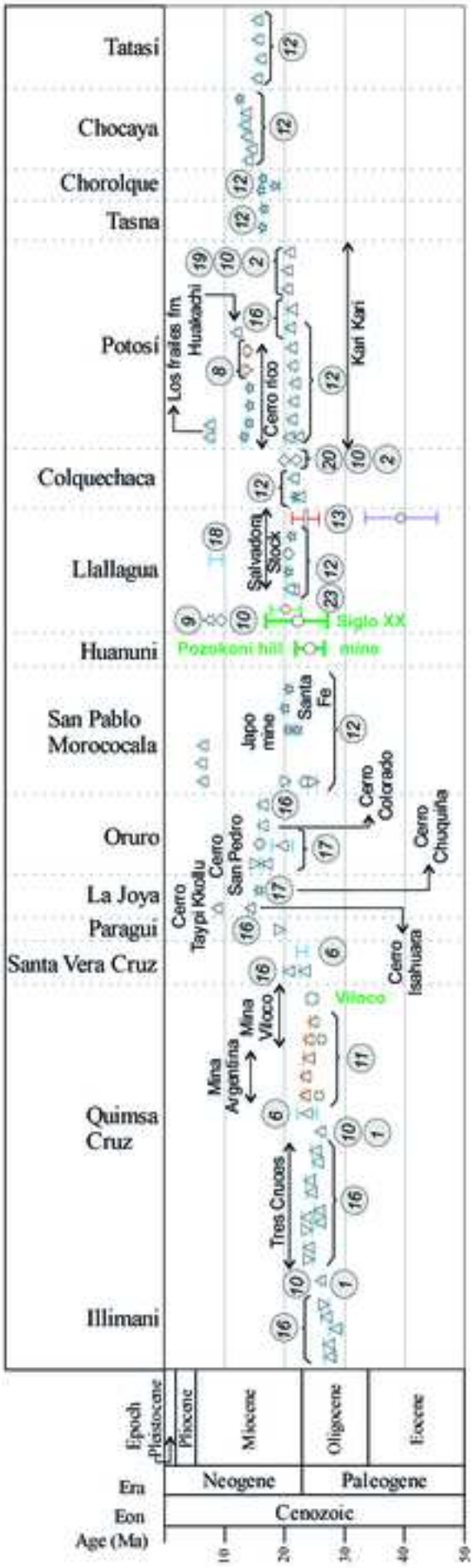

Supplementary Figure S1

Supplementary Figure S2

Supplementary Figure S3